JℲM PAPERS

Reynolds number dependence of turbulent flows over a highly permeable wall

Y. Kuwata[1],† **and K. Suga**[1]

[1]Department of Mechanical Engineering, Osaka Metropolitan University, Sakai, Osaka 599-8531, Japan

Direct numerical simulations of turbulent flows over highly permeable porous walls were performed at various Reynolds numbers to examine the effects of the Reynolds number on permeable wall turbulence. The porous medium consisted of Kelvin cell arrays with porosity 0.95, and the permeability Reynolds number Re_K ranged from approximately 7 to 50. Simulations with thin and thick porous walls were performed to investigate the effects of spanwise roller vortices associated with the Kelvin–Helmholtz instability. The results show that the effect of the Kelvin–Helmholtz instability becomes more significant with increasing the permeability Reynolds number, and spanwise rollers, for which length scale is an order of channel height, dominate turbulence when $Re_K \gtrsim 30$. Spanwise rollers reinforce the negative correlation between the wall-normal and streamwise velocity fluctuations close to the porous/fluid interface, and intensify the turbulent velocity fluctuations away from the porous walls, leading to increased frictional resistance. An investigation of the Reynolds number dependence of the modified logarithmic law indicates that the zero-plane displacement and equivalent roughness height are proportional to the square root of permeability, whereas the von Kármán constant increases with the permeability Reynolds number because of the increased mixing length resulting from the relatively large-scale velocity fluctuations induced by spanwise rollers. We developed a model for the modified log law for permeable wall turbulence based on permeability, and confirmed that the skin friction coefficient obtained from the model reasonably predicts the skin friction coefficient for several types of high-porosity porous media. Hence, permeability is a key parameter that characterizes the logarithmic mean velocity profiles over a variety of porous media with high porosity.

Key words: porous media, turbulence simulation, turbulent boundary layers

† Email address for correspondence: ykuwata1919@gmail.com

1. Introduction

Turbulent flows over permeable porous walls have attracted considerable scientific and engineering interest because of the considerably enhanced momentum, heat and mass transfer across the porous/fluid interface. In engineering applications, porous media are encountered in the gas diffusion layers of proton-exchange membrane fuel cells, catalytic converters for automobile exhaust systems, transpiration cooling systems, and heat exchangers. In the context of the geophysical and environmental fields, flows over vegetation and urban canopies (Finnigan 2000; Nepf & Ghisalberti 2008), and natural river beds (Detert, Nikora & Jirka 2010), are affected by roughness and permeability.

One of the most notable characteristics of turbulent flows over permeable porous walls that distinguishes the permeable wall turbulence from the rough wall turbulence is the presence of spanwise roller vortices associated with the Kelvin–Helmholtz (K–H) instability. It has been reported that spanwise roller vortices can develop over various walls, such as foam media (Suga *et al.* 2010), cube arrays (Breugem & Boersma 2005; Kuwata & Suga 2016*b*), longitudinal ribs (Garcia-Mayoral & Jiménez 2012; Kuwata 2022*a*), vegetation canopies (Finnigan 2000; White & Nepf 2007), and packed beds (Guan *et al.* 2021), as well as rough walls (Stoesser *et al.* 2008; García-Mayoral & Jiménez 2011; Endrikat *et al.* 2021), vegetation canopies (Finnigan 2000; White & Nepf 2007), and elastic walls (Rosti & Brandt 2017; Jha & Steinberg 2021). In contrast with the quasi-streamwise vortices in the near-wall turbulence, spanwise rollers accompany relatively large-scale sweep and ejection motions, leading to a significantly enhanced momentum transfer (Breugem, Boersma & Uittenbogaard 2006; Kuwata & Suga 2016*b*) and heat transfer (Nishiyama, Kuwata & Suga 2020) across the porous/fluid interface. In addition, because the characteristic length scale for spanwise rollers is comparable to the boundary layer thickness (Kuwata & Suga 2017; Suga *et al.* 2018) or shear length scale (Finnigan 2000; White & Nepf 2007), the effect of spanwise rollers has not been confined to the vicinity of the porous/fluid interface but extends into the logarithmic region or beyond the boundary layer (Kuwata & Suga 2019), which results in a modification of the von Kármán constant (Poggi *et al.* 2004; Kuwata 2022*b*).

To approximate the mean velocity profiles over permeable porous walls, customarily the modified logarithmic law (log law) is used:

$$U^{p+} = \frac{1}{\kappa} \ln \left(\frac{y + d_p}{h_r} \right), \tag{1.1}$$

where κ, d_p and h_r are the von Kármán constant, the zero-plane displacement and the equivalent roughness height, respectively. The streamwise mean velocity U with a superscript '$p+$' stands for the mean velocity normalized by the friction velocity at the porous/fluid interface. Because the von Kármán constant κ does not necessarily coincide with the standard value for smooth-wall turbulence, three unknown log-law parameters, κ, d_p, and h_r, must be determined to approximate the mean velocity profiles. With respect to d_p and h_r, the direct numerical simulations (DNS) studies by Kuwata & Suga (2017) reported a close correlation between d_p and h_r, regardless of the Reynolds number. An experimental study of a turbulent boundary layer over a highly permeable metal foam by Esteban *et al.* (2022) showed that d_p and h_r are related closely to the pore size, whereas experiments on foam media in Suga *et al.* (2010) and Manes, Poggi & Ridol (2011) showed that d_p and h_r are expressed as functions of the square root of permeability $\sqrt{K}$. Here, the permeability K for isotropic porous media is defined in low Reynolds number fully

developed porous medium flows, that is, Darcy flow (Whitaker 1986):

$$-\frac{1}{\rho}\frac{\partial P}{\partial x} = \nu K^{-1} U_d, \qquad (1.2)$$

where ν and P are the kinematic viscosity and pressure, respectively. Darcian velocity U_d is defined as the superficially averaged velocity over a representative elementary volume. The parametrization of d_p and h_r was extended to anisotropic porous media by introducing a pore length scale at the porous/fluid interface (Suga *et al.* 2018). Therefore, there is consensus that the flow properties of d_p and h_r are related to the physical length scales of porous media. However, the value of the von Kármán constant is controversial. Esteban *et al.* (2022) showed that the standard value for smooth-wall turbulence can be used straightforwardly for turbulent boundary layers over metal foams. This concept is common in vegetation canopies (Nepf & Ghisalberti 2008). In contrast, DNS (Breugem *et al.* 2006; Kuwata & Suga 2016*b*; Chu *et al.* 2021) and experimental studies (Suga *et al.* 2010, 2018; Manes *et al.* 2011) have determined κ by collapsing the U^{p+} profiles into the modified log law of (1.1) and suggested a considerably smaller κ value than the standard value for smooth-wall turbulence. However, considering that the Reynolds numbers in most of these studies were not sufficiently high to guarantee the logarithmic mean velocity profiles, the direct fit of the U^{p+} profiles to the log law may be problematic. To avoid this problem, Kuwata (2022*b*) employed a different method for determining κ, d_p and h_r based on the Jackson model (Jackson 1981) where d_p is defined as the level at which the mean drag by the permeable walls acts. Kuwata (2022*b*) reported that the von Kármán constant becomes larger than the smooth-wall value owing to an increase in the mixing length by spanwise rollers.

Because the skin friction coefficient C_f^p at the porous/fluid interface is related directly to the U^{p+} profile, exploring the scaling of C_f^p as an alternative to logarithmic mean velocity profiles is crucial. Earlier studies were conducted on relatively dense porous media, such as packed beads (Ho & Gelhar 1973) and sand beds (Lovera & Kennedy 1969). They showed that C_f^p increases with the Reynolds number, even within the fully rough regime, where the friction factor is normally independent of the Reynolds number. However, this is not true for highly permeable porous media (Suga *et al.* 2010; Esteban *et al.* 2022). Esteban *et al.* (2022) systematically measured turbulent boundary layers over metal foam with varying pore sizes and permeabilities across a broad range of friction Reynolds numbers, from $Re_\tau \simeq 2000$ to $Re_\tau \simeq 18\,000$. They found that C_f^p depends on the characteristics of the porous substrates and reaches a plateau beyond $Re_\tau \simeq 5000$. A similar observation was reported in a recent DNS study using modified wall boundary conditions (Motoki *et al.* 2022), where the wall-normal transpiration velocity is assumed to be proportional to the local pressure fluctuation, as reported by Jiménez *et al.* (2001). They reported that C_f^p takes a constant value in the sufficiently high Reynolds number regime, where spanwise rollers with large-scale wall blowing and suction dominate the boundary layer.

Despite extensive research conducted over the last several decades, there is a lack of consensus regarding the scaling of the mean velocity profiles over permeable walls. In particular, the value of the von Kármán constant is controversial, which may be affected by spanwise roller vortices associated with the K–H instability. The objective of this study was to unveil the Reynolds number dependence on the emergence of the K–H instability, and the consequent effects on the mean flow characteristics over permeable walls. Particular attention was paid to the effects of spanwise rollers, which do not develop for low-permeability Reynolds number $Re_K = \sqrt{K} u_\tau / \nu$ flows but dominate turbulence for high Re_K flows (Breugem *et al.* 2006; Kuwata & Suga 2019). Hence we considered

the turbulence over high-porosity porous media over a wide range of Reynolds number, leading to $Re_K \simeq 7$–50, which covers low to considerably higher Re_K flows than in previous DNS studies (Breugem *et al.* 2006; Chu *et al.* 2021; Kuwata 2022*b*). An in-depth discussion on the role of spanwise rollers was conducted by performing DNS for thick and thin porous walls, where effectively the thin porous wall attenuates the velocity fluctuations associated with the K–H instability (Kuwata & Suga 2016*b*).

2. The DNS methodology

2.1. *Flow conditions and computational details*

Following the DNS study by Kuwata (2022*b*), we considered fully developed turbulent flows through a channel partially filled with arrays of Kelvin cells (polyhedra with six square and eight hexagonal faces Thomson 1887). Although we adopted the same computational method as that used by Kuwata (2022*b*), we explain it briefly for comprehensiveness (a full description of the numerical methodology is provided in the study performed by Kuwata 2022*b*). The sketch depicting the flow configuration is shown in figure 1, where H and h denote the channel and porous wall heights, respectively. The top and bottom walls were impermeable smooth walls, and we considered arrays of Kelvin cells in $-h < y < 0$ as shown in figure 2(*a*) to mimic highly permeable foam media. The choice of asymmetric wall boundary conditions is consistent with those reported by DNS studies (Jiménez *et al.* 2001; Breugem *et al.* 2006; Kuwata & Suga 2016*b*; Chu *et al.* 2021), and may yield results comparable to those of boundary layer flow experiments for porous walls (Suga *et al.* 2010; Manes *et al.* 2011) and vegetation canopies (Finnigan 2000; Nepf & Ghisalberti 2008). We did not select a channel with two parallel porous walls to avoid interactions between spanwise rollers originating from the two parallel walls because the effect of spanwise rollers over permeable walls usually extends beyond the boundary layer (Kuwata & Suga 2019).

The porosity of the porous wall was $\varphi = 0.95$, and the size of a single unit of the Kelvin cell was set to $L = H/3$, which yielded permeability $K/H^2 = 1.9 \times 10^{-3}$. Here, porosity is the volume fraction of the fluid phase over the representative elementary volume, while permeability is a flow parameter that quantifies easiness of flow through porous media. In this study, porosity is defined as the volume fraction of the fluid phase within a single unit of the Kelvin cell, and the permeability is computed by a relation between pressure drop and Darcian velocity in low Reynolds number fully developed porous medium flows using (1.2).

The flow was periodic in the streamwise (x) and spanwise (z) directions. Simulations were run by imposing a mean streamwise pressure difference. The mean pressure difference was varied such that the friction Reynolds numbers based on the average friction velocity u_τ and channel height H were varied: $Re_\tau = 141, 331, 626$ and 955 (the definition of u_τ is given in § 2.2.)

To examine the effects of spanwise rollers, we considered thick ($h = H$) and thin ($h = H/3$) porous walls, as shown in figure 1. A precursor study by Kuwata (2022*b*) confirmed that for the present porous media, spanwise rollers are attenuated for the thin porous wall with $h = H/3$, because the smooth wall beneath the thin porous substrate attenuates the vertical transpiration velocity at the porous/fluid interface. Therefore, eight simulation cases with different friction Reynolds numbers and wall thicknesses were considered. In the following, for the sake of brevity, cases were named as follows: 'A-B', where 'A' denotes the friction Reynolds number, and 'B' is either 'thin' ($h = H/3$) or 'thick' ($h = H$). The size of the computational domain of $L_x(x) \times (H + h)(y) \times L_z(z)$ was
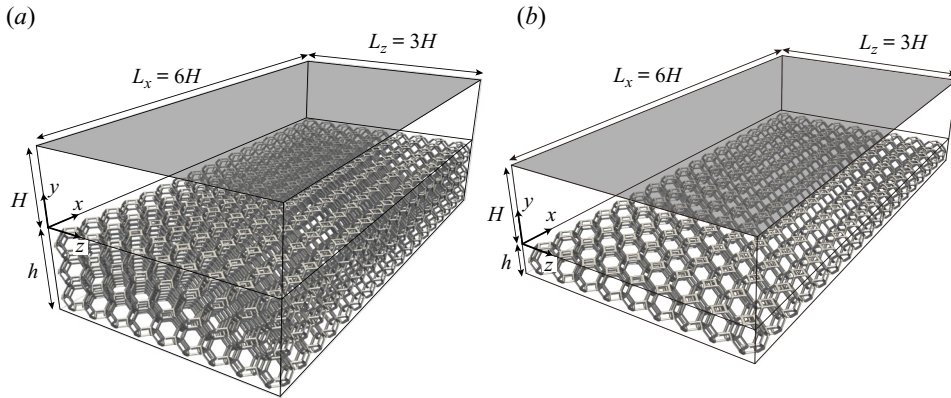
Figure 1. Computational geometry of the porous-walled channel flows: (*a*) thick-walled case ($h = H$) and (*b*) thin-walled case ($h = H/3$). The porous wall consists of Kelvin cell arrays with porosity 0.95, and the top and bottom walls are impermeable smooth walls. Note that a double spanwise domain length $L_z = 6H$ is considered for cases 626-thick and 955-thick.

$L_x = 6H$ and $L_z = 3H$, except for cases 626-thick and 955-thick, where we considered double the spanwise domain length, $L_z = 6H$, to accommodate large-scale spanwise rollers. The size of the domain is comparable to or larger than that used in previous DNS studies on porous-walled channel flows (Jiménez *et al.* 2001; Breugem *et al.* 2006; Chandesris *et al.* 2013) and was confirmed to be sufficient to accommodate spanwise rollers associated with the K–H instability.

For the numerical method, following previous studies (Kuwata 2022*b*), we utilized the three-dimensional 27-velocity multiple-relaxation-time lattice Boltzmann method (Suga *et al.* 2015) with the imbalance-correction local grid refinement technique proposed by Kuwata & Suga (2016*a*). The numerical method was validated against canonical turbulent flows (Suga *et al.* 2015), and we confirmed that the results were in good agreement with the experimental data for turbulent flows over porous walls (Kuwata & Suga 2017; Kuwata, Tsuda & Suga 2020). Based on the recommendations for wall-bounded flows of Suga *et al.* (2015), the grid resolution of the equidistant regular grid near the porous wall was determined such that the grid spacing was approximately $\Delta^{p+} < 2.5$, where Δ^{p+} denotes the grid spacing of the fine grid block normalized with the friction velocity at the porous/fluid interface u_τ^p (the definition of u_τ^p is provided in §2.2). This resolution constraint was confirmed as valid for the present flow geometry (Kuwata 2022*b*). In addition, to ensure the grid independence of the solutions, a grid sensitivity test was performed for case 955-thick. A comparison of a coarser mesh with $\Delta^{p+} = 2.9$ and a finer mesh with $\Delta^{p+} = 2.1$ yielded a change in the skin friction coefficient of approximately 2.6 %, confirming that the current resolution with $\Delta^{p+} = 2.4$ is sufficiently fine to obtain grid-independent solutions. In addition, the following constraint was imposed: a cross-section of a circular ligament of the Kelvin cell must be resolved using at least 8×8 grids to accurately resolve the geometry of the Kelvin cells. Figure 2(*b*) depicts typical *x–y* plane velocity vectors around a ligament for this resolution (case 141-thick), showing that the flow around a ligament appears to be simulated reasonably. We confirmed that this resolution was sufficient to reproduce correctly the hydraulic characteristics of the flow through a Kelvin cell with $\varphi = 0.95$ at $Re_d < 25$; doubling the number of grid points in each direction yields changes in the permeability and Forchheimer coefficient of
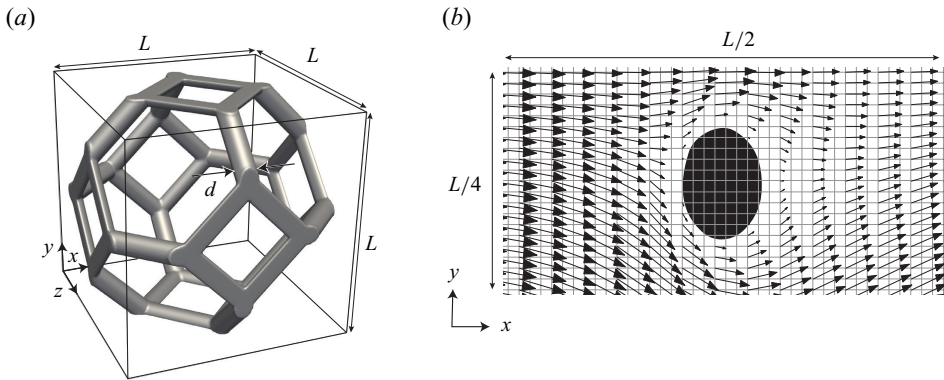
(*a*)

(*b*)

Figure 2. (*a*) Geometry of a single unit of a Kelvin cell with porosity 0.95. (*b*) Typical *x*–*y* plane velocity vectors and grid around a ligament at $z = L/4$ for case 141-thick. Here, L denotes the size of the Kelvin cell, and d is the diameter of the circular ligament of the Kelvin cell. The velocity vectors are reduced by skipping every two points in the x direction.

Case	Re_τ	h/H	Grid points (fine) $(x \times y \times z)$	Grid points (coarse) $(x \times y \times z)$	Δ^{p+}	d/Δ	L/Δ
141-thick	141	1	$1440 \times 304 \times 720$	$720 \times 90 \times 360$	0.7	7.3	80
141-thin	141	1/3	$1440 \times 144 \times 720$	$720 \times 90 \times 360$	0.7	7.3	80
331-thick	331	1	$1440 \times 304 \times 720$	$720 \times 90 \times 360$	1.7	7.3	80
331-thin	331	1/3	$1440 \times 144 \times 720$	$720 \times 90 \times 360$	1.7	7.3	80
626-thick	626	1	$1979 \times 375 \times 1979$	$990 \times 144 \times 990$	2.4	10	110
626-thin	626	1/3	$1979 \times 155 \times 990$	$990 \times 144 \times 495$	2.3	10	110
955-thick	955	1	$3239 \times 589 \times 3239$	$1620 \times 248 \times 1620$	2.3	16.4	180
955-thin	955	1/3	$3239 \times 229 \times 1620$	$1620 \times 248 \times 810$	2.2	16.4	180

Table 1. Parameters of the simulations. We considered eight simulations with different friction Reynolds numbers Re_τ and wall thickness h/H. Here, Δ^{p+} is the grid spacing for the fine grid block normalized with u_τ^p, d denotes the diameter of the circular ligament of the Kelvin cell, and L/Δ denotes the number of grid points for resolving a single Kelvin cell unit in each direction.

approximately 2 % and 5 %, respectively. Here, Re_d is the Reynolds number based on the Darcian velocity U_d and ligament diameter d.

The parameters of the simulations regarding the grid are presented in table 1. Notably, we allocated the twice-coarser grids away from the porous wall using a grid-refinement technique (Kuwata & Suga 2016*a*) to circumvent prohibitively high computing resources for handling the entire computational domain with a single-grid resolution. The interface between the fine and coarse grid blocks was located $100\Delta^{p+}$ off the porous wall at $Re_\tau = 331$, 626 and 955, while the interface was located at $y = 0.27H$ for the lowest Re_τ cases.

2.2. *Flow characteristic parameters*

For a porous-walled channel flow where the flow is bounded by a bottom porous wall and top smooth wall, two friction velocities can be defined: the friction velocity at the porous/fluid interface u_τ^p, and that at the smooth wall u_τ^s. For the top smooth wall, we can directly compute the shear stress at the wall τ_w^s, and the friction velocity is given by

$u_\tau^s = \sqrt{\tau_w^s/\rho}$. The shear stress at the porous/fluid interface is obtained from the streamwise momentum balance between the pressure drop ΔP and $\tau_w^p = \rho(u_\tau^p)^2$ as in Kuwata & Suga (2016*b*):

$$L_x L_z (\tau_w^p + \tau_w^s) = H L_z \, \Delta P. \qquad (2.1)$$

This yields

$$\tau_w^p = H \frac{\Delta P}{L_x} - \tau_w^s. \qquad (2.2)$$

Notably, τ_w^s denotes viscous shear stress at the top wall, while τ_w^p corresponds to the total shear stress at the porous/fluid interface, including the viscous, turbulent and dispersion stresses. The definition of τ_w^p is comparable to those used in previous experiments (Manes *et al.* 2009; Suga *et al.* 2010). The average wall shear stress $u_\tau = \sqrt{\tau_w/\rho}$ is given by the average wall shear stress $\tau_w = (\tau_w^p + \tau_w^s)/2$, which is related to the streamwise pressure difference:

$$\tau_w = \frac{H}{2} \frac{\Delta P}{L_x}. \qquad (2.3)$$

Hence, simulations with the same friction Reynolds number have the same pressure difference. Note that because the wall thickness does not alter τ_w^s significantly at the top wall, simulations with the same Re_τ prescribe almost the same τ_w^p at the porous/fluid interface (a maximum difference in the viscous wall unit of approximately 5 %). In the following, we discuss the non-dimensionalized values with the average friction velocity u_τ, friction velocity at the porous/fluid interface u_τ^p, and friction velocity at the smooth wall u_τ^s, which are denoted by values with superscripts '+', '$p+$' and '$s+$', respectively. We chose normalization with u_τ to discuss the turbulence modification at a given pressure difference, and consider the values non-dimensionalized with u_τ^p and u_τ^s in discussing the scaling of the turbulence statistics for the porous and smooth-wall sides, respectively. The difference between the top and bottom walls results in an asymmetry in the mean velocity profile in the clear flow region of $0 < y < H$. The boundary layer thickness for the porous wall side is defined as the distance from the porous/fluid interface to the location where the total shear stress becomes zero (Breugem *et al.* 2006). Given that the total shear stress profile in the clear flow region is linear with respect to y, the boundary layer thickness for the porous wall side δ_p is given as

$$\delta_p = \frac{\tau_w^p}{\tau_w^s + \tau_w^p} H. \qquad (2.4)$$

2.3. *Averaging procedure*

For a fully developed turbulent channel flow bounded by a smooth wall, the turbulence statistics vary one-dimensionally along the wall-normal direction. However, this is not the case for the porous wall because the wall geometry is inhomogeneous in the streamwise and spanwise directions. Hence, following the previous DNS studies (Kuwata 2022*b*), we introduce the spatial averaging of variable ϕ in the x–z plane as

$$\langle \phi \rangle (y, t) = \frac{1}{A} \int_{x_f} \int_{z_f} \phi(x, y, z, t) \, dx \, dz, \qquad (2.5)$$

where x_f and z_f denote the positions in the fluid phase, $A = L_x L_z$, and $\langle \phi \rangle$ represents the superficial average value. The intrinsic (fluid phase) average value is $\langle \phi \rangle^f = (A/A_f) \langle \phi \rangle$,

Case	Re_τ	h/H	Re_τ^p	Re_b	Re_K	$C_f^p \times 10^{-2}$	$C_f^s \times 10^{-2}$
141-thick	141	1	117	1460	7.2	5.1	2.2
141-thin	141	1/3	114	1561	7.2	4.2	1.9
331-thick	331	1	315	4048	17.8	4.8	1.5
331-thin	331	1/3	300	4431	17.5	3.6	1.3
626-thick	626	1	647	7921	34.7	5.3	1.3
626-thin	626	1/3	581	9144	33.2	3.2	1.0
955-thick	955	1	1013	12 480	52.8	5.3	1.1
955-thin	955	1/3	912	14 608	51.0	3.1	0.9

Table 2. Global flow characteristic parameters: $Re_\tau^p = \delta_p u_\tau^p/\nu$ is the friction Reynolds number for the porous wall side; $Re_b = U_b H/\nu$ is the bulk mean Reynolds number; $Re_K = \sqrt{K}\, u_\tau^p/\nu$ is the permeability Reynolds number; $C_f^p = \tau_w^p/(\rho U_b^2)$ and $C_f^s = \tau_w^s/(\rho U_b^2)$ are the skin friction coefficients for the porous and smooth walls, respectively.

which involves averaging over the x–z plane occupied by the fluid phase, and dispersion from the intrinsically averaged value is denoted by $\tilde{\phi} = \phi - \langle\phi\rangle^f$, where A_f denotes the area of the x–z plane within the fluid phase. As the variable also fluctuates in time, we consider Reynolds averaging over time. The Reynolds-averaged value of the variable ϕ is denoted as $\bar{\phi}$, and ϕ' denotes the fluctuation from the Reynolds-averaged value: $\phi' = \phi - \bar{\phi}$. For Reynolds averaging, the statistics were accumulated over approximately $4L_x/u_\tau^p$ for the cases at $Re_\tau = 955$, and $40L_x/u_\tau^p$ for the cases at $Re_\tau = 141$.

3. Results and discussion

3.1. *Skin friction coefficient*

Before discussing the profiles of the turbulence statistics, we briefly examine how porous walls affect the general flow characteristics. Table 2 lists the friction Reynolds number for the porous wall side, $Re_\tau^p = \delta_p u_\tau^p/\nu$, the bulk mean Reynolds number $Re_b = U_b H/\nu$, the permeability Reynolds number $Re_K = \sqrt{K}\, u_\tau^p/\nu$, and skin friction coefficients for the porous wall $C_f^p = \tau_w^p/(\rho U_b^2)$ and the smooth wall $C_f^s = \tau_w^s/(\rho U_b^2)$. Here, the bulk mean velocity U_b is defined as $U_b = Q_c/H$, where Q_c is the flow rate in the clear flow region, $0 < y < H$. The trends of C_f^p and C_f^s are also shown in figure 3 to facilitate understanding of the effects of Re_τ and h/H. Figure 3(*a*) shows that C_f^p is larger than C_f^s, as expected. Notably, C_f^p for thin-wall cases decreases consistently with Re_τ, whereas C_f^p for the thick cases exhibits an increase trend when Re_τ increases from 331 to 626. Given that Re_K in table 2 is significantly higher than the threshold value 3.0 (Suga *et al.* 2010), an increase in C_f^p is attributed to the combined effects of wall roughness and permeability. Another observation is that C_f^p for thick-wall cases tends to converge to a certain value at a higher Re_τ, which is similar to the DNS results for turbulent channel flows with modelled permeable walls (Motoki *et al.* 2022) as well as experiments for ceramic foams (Suga *et al.* 2010) and metal foams (Esteban *et al.* 2022).

When attention is given to the effects of the wall thickness h/H, we observe from figure 3(*a*) that both C_f^p and C_f^s are larger for the thick-wall cases. An increase in C_f^p with wall thickness has also been reported in previous DNS studies (Kuwata & Suga 2016*b*) and experiments (Zippe & Graf 1983; Manes *et al.* 2009). As a result, the thickening of the wall
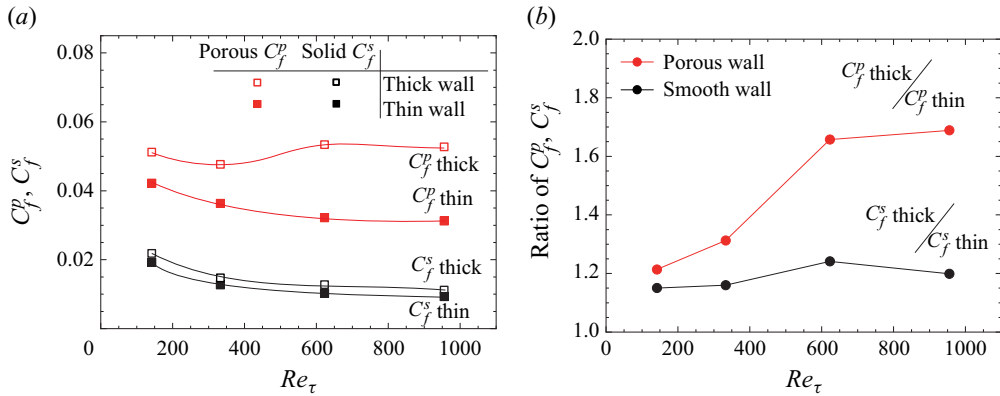
Figure 3. Skin friction coefficients at the porous/fluid interface (C_f^p) and at the smooth wall (C_f^s) against Re_τ: (*a*) C_f^p and C_f^s for the thick- and thin-wall cases, and (*b*) the ratios of C_f^p and C_f^s for the thick-wall cases divided by the corresponding values for the thin-wall cases.

increases Re_τ^p but decreases Re_b, as shown in table 2. The effects of wall thickness on the skin friction coefficient are illustrated in figure 3(*b*), where C_f^p and C_f^s for the thick-wall cases are divided by the corresponding values for the thin-wall cases. Figure 3(*b*) confirms that the effects of the wall thickness exhibit Reynolds number dependence; the ratio of C_f^p increases abruptly with Re_τ up to $Re_\tau \simeq 600$, whereas a further increase in Re_τ diminishes this increasing trend. Interestingly, as shown in figure 3(*b*), the thickening of the wall also increases C_f^s. This implies that the effects of wall thickness may reach the other side of the top smooth wall. The underlying physics of the modification of C_f^p and C_f^s is discussed in the following subsections.

3.2. *Spanwise rollers*

As argued earlier, turbulent flows over a permeable porous wall are characterized by the presence of spanwise rollers associated with the K–H instability. Here, we focus on the effect of the Reynolds number on the presence of spanwise rollers. Figure 4 shows snapshots of streamwise velocity fluctuations normalized by u_τ^p above a porous wall at $y^{p+} \simeq 10$. For all cases, the streamwise elongated high- and low-speed streaks are disrupted by wall roughness or permeability, and the footprints of small-scale eddies, which scale with viscous wall units ν/u_τ^p, decrease with increasing Re_τ. More importantly, for the thick-wall cases, with the exception of the lowest Re_τ case, the high- and low-speed regions tend to merge, and are considerably larger than those in the thin-wall cases. This unique turbulence structure may be responsible for the K–H instability, which usually occurs for turbulence over permeable walls (Jiménez *et al.* 2001; Breugem *et al.* 2006; Kuwata & Suga 2016*b*), rough walls (Stoesser *et al.* 2008; García-Mayoral & Jiménez 2011; Endrikat *et al.* 2021), vegetation canopies (Finnigan 2000; White & Nepf 2007) and elastic walls (Rosti & Brandt 2017; Jha & Steinberg 2021). In particular, the turbulence structure for case 955-thick is similar to that in the experiments on turbulence over ceramic foam (Suga, Nakagawa & Kaneda 2017; Suga *et al.* 2018) although the spanwise coherence is visually weaker than reported by the DNS studies (Jiménez *et al.* 2001; Kuwata & Suga 2019; Endrikat *et al.* 2021). The reduction in spanwise coherence is likely due to the Reynolds number effects reported by Kuwata & Suga (2019), who showed that the

spanwise-connected high- and low-speed regions became less obvious with increasing Re_K.

Qualitative discussions of the effects of wall thickness on the turbulence structures are made with figure 5, which presents two-dimensional pre-multiplied cospectra of the streamwise and wall-normal velocity fluctuations at $y^{p+} \simeq 10$. For the lowest Re_τ cases, we see that the energy spectra for cases 141-thick and 141-thin are visually similar. However, the energy spectra in the wavelength regions $\lambda_x/\delta_p \simeq 4$ and $\lambda_z/\delta_p \simeq 3$ appear to be more energetic for the thick-wall case. This trend is more pronounced for the higher Re_τ cases (626-thick and 955-thick). For cases 626-thick and 955-thick, the energy spectra are dominated by the velocity fluctuations associated with this wavelength region. Note that the more energetic region compared with the thin-wall results is approximately $\lambda_x/\delta_p \simeq 4$, which corresponds approximately to the characteristic wavelength of the K–H instability, with $\lambda_x/\delta_p \simeq 3$–5.5 (Kuwata & Suga 2017; Suga *et al.* 2018), $\lambda_x/\delta_p \simeq 1.5$–3 (Manes *et al.* 2011) and $\lambda_x/\delta_p \simeq 1$–5 (Efstathiou & Luhar 2018). Therefore, for the present permeable wall, the turbulent structure associated with the K–H instability develops for the thick-wall cases; the effects of the K–H instability are weak at the lowest Re_τ (case 141-thick), whereas the velocity fluctuations associated with the K–H instability dominate turbulence at higher Re_τ (cases 626-thick and 955-thick). However, it should be cautioned that not only the wall thickness but also the wall characteristic parameters related to flow resistance and deformation are key parameters for the occurrence of the K–H instability (Jiménez *et al.* 2001; White & Nepf 2007; Rosti & Brandt 2017). Indeed, the spanwise rollers develop over the riblets of Endrikat *et al.* (2021) and elastic walls of Rosti & Brandt (2017), which are considerably thinner than the thin walls used in this study. Notably, for cases 626-thick and 955-thick, the energetic regions $\lambda_x/\delta_p \simeq 4$ and $\lambda_z/\delta_p \simeq 3$ remain unchanged by the Reynolds number. The corresponding large-scale motions for case 955-thick are visualized in figure 6, where the spanwise average over $0 < z < 3\delta_p$ is applied to the velocity fluctuations to facilitate clear inspection of large-scale motions (Suga *et al.* 2018; Motoki *et al.* 2022). We observe large-scale spanwise roller motion with a streamwise extent of approximately $\lambda_x/\delta_p \simeq 3$–4. Visual inspection shows that this may be the maximum possible size of spanwise rollers that can be accommodated in a porous-walled channel. This may be why an increase in Re_τ from 626 to 955 does not alter the energy spectra significantly. In this sense, the turbulence for cases 626-thick and 955-thick can be referred to as the 'ultimate porous wall turbulence regime'. The maximum possible size of the spanwise rollers depends on the flow configuration. The sizes of spanwise rollers scale principally with shear length scales (Finnigan 2000; White & Nepf 2007); however, the sizes of spanwise rollers are restricted by the flow confinement, such as the flow depth for gravel flows (Roy *et al.* 2004; Manes *et al.* 2011) and vegetation height for canopy flows (Nepf & Vivoni 2000).

To better understand the contribution of spanwise rollers to the Reynolds shear stress in the clear flow region, following Endrikat *et al.* (2021), we analyse the Reynolds shear stress contributed by relatively large-scale velocity fluctuations:

$$R_{12,L}(y) = \int_{1/L_x}^{\kappa_x^*} \int_{1/L_z}^{\kappa_z^*} E_{uv}(y) \, \mathrm{d}\kappa_x \, \mathrm{d}\kappa_z, \tag{3.1}$$

where the choices of κ_x^* and κ_z^* are arbitrary; we use $\kappa_x^* = \kappa_z^* = 2/(3H)$, which corresponds to wavelength approximately $2\delta_p$. That is, $R_{12,L}$ consists of the velocity fluctuations in the wavelength regions $\lambda_x \gtrsim 2\delta_p$ and $\lambda_z \gtrsim 2\delta_p$, which covers the characteristic scale of spanwise rollers $\lambda_x \simeq 4\delta_p$ and $\lambda_z \simeq 3\delta_p$. However, $R_{12,L}$ may
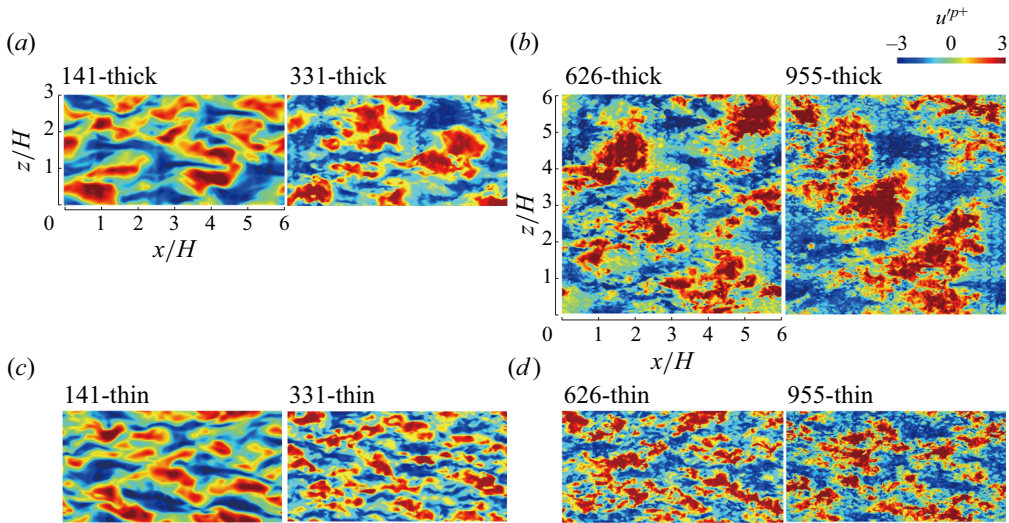
Figure 4. Snapshots of streamwise velocity fluctuations $u'^{p+} = u'/u_\tau^p$ at $y^{p+} \simeq 10$. The friction Reynolds number increases from left to right. Results for the (a,b) thick-wall and (c,d) thin-wall cases.
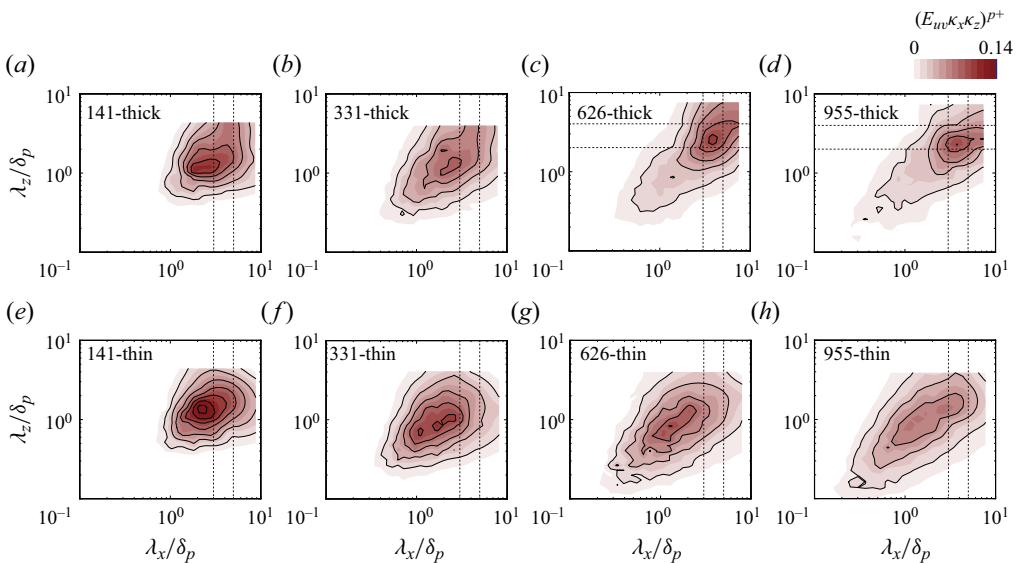

Figure 5. Two-dimensional pre-multiplied cospectra of streamwise and wall-normal velocity fluctuations $(E_{uv}\kappa_x\kappa_z)^{p+}$ at $y^{p+} \simeq 10$. The friction Reynolds number increases from left to right. The top and bottom rows show the results for the thick- and thin-wall cases, respectively. The thin dashed lines indicate $\lambda_x/\delta_p = 3$ and 5, $\lambda_z/\delta_p = 2$ and 4.

not represent perfectly the contribution of spanwise rollers, but also contains velocity fluctuations associated with irrelevant large-scale perturbations. The contributions of relatively large-scale velocity fluctuations to the Reynolds shear stress are shown in figure 7. Evidently, no major difference was observed between $-R_{12}^{p+}$ for the thick- and thin-wall cases, whereas the effects of wall thickness are distinctly visible in the
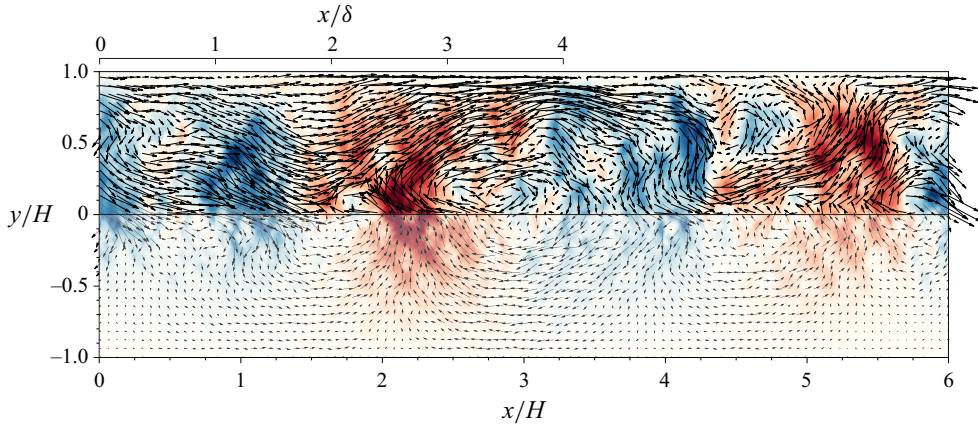
Figure 6. Snapshots of velocity fluctuations averaged over $0 < z < 3\delta_p$ for case 955-thick. The contour shows the spanwise-average wall-normal velocity fluctuations. The blue and red contours indicate $v'^{p+} = -0.5$ and $+0.5$, respectively.

decomposed Reynolds shear stress $-R_{12,L}^{p+}$. In figures 7(a,c), $-R_{12,L}^{p+}$ for the thick-wall cases occupies a large portion of $-R_{12}^{p+}$ for the porous wall side, and the dominance of $-R_{12}^{p+}$ is more pronounced at $Re_\tau = 955$ (case 955-thick). Considering that relatively large-scale fluctuations are associated mostly with spanwise rollers owing to K–H instability, we can deduce that spanwise rollers contribute to the enhancement of the Reynolds shear stress. This is the leading cause of the increase in C_f^p with the Reynolds number for the thick-wall cases. Indeed, for the thick-wall cases, the augmentation of C_f^p with respect to the thin-wall case is more pronounced with the enhancement of the energy spectra around $\lambda_x \simeq 4\delta_p$ and $\lambda_z \simeq 3\delta_p$. In the 'ultimate porous wall turbulence regime' for cases 626-thick and 955-thick, where the dominance of the velocity fluctuations associated with the K–H instability is saturated, C_f^p is almost independent of the Reynolds number.

3.3. *Effects of spanwise rollers on Reynolds stress*

The above discussion confirms that spanwise rollers are the root cause of the increased C_f^p for thick-wall cases. This subsection focuses on how spanwise rollers augment momentum transfer. Figure 8 shows the streamwise and wall-normal turbulence intensities, $\sqrt{R_{11}}$ and $\sqrt{R_{22}}$, respectively, normalized by the average friction velocity u_τ, where the Reynolds stress is defined as $R_{ij} = \langle \overline{u_i' u_j'} \rangle$. For the clear flow region $0 < y/H < 1$, the maximum peak values of the turbulence intensities near the porous/fluid interface are unaffected by the wall thickness. However, away from the porous wall, the thickening of the wall tends to increase the turbulence intensity. An increase in $\sqrt{R_{22}}^+$ is observed in a large portion of the clear flow region, $0.2 < y/H < 0.9$, whereas an increase in $\sqrt{R_{11}}^+$ is notable at approximately $y/H \simeq 0.8$. The enhanced turbulence intensities away from the wall are pronounced for cases 626-thick and 955-thick where spanwise rollers dominate the turbulence.

The second moments that contribute to the momentum transfer are shown in figure 9, which depicts the Reynolds shear stress R_{12} and dispersive covariance $T_{12} = \langle \tilde{u}\tilde{v} \rangle$. In addition, we plot the correlation coefficient for the Reynolds shear stress
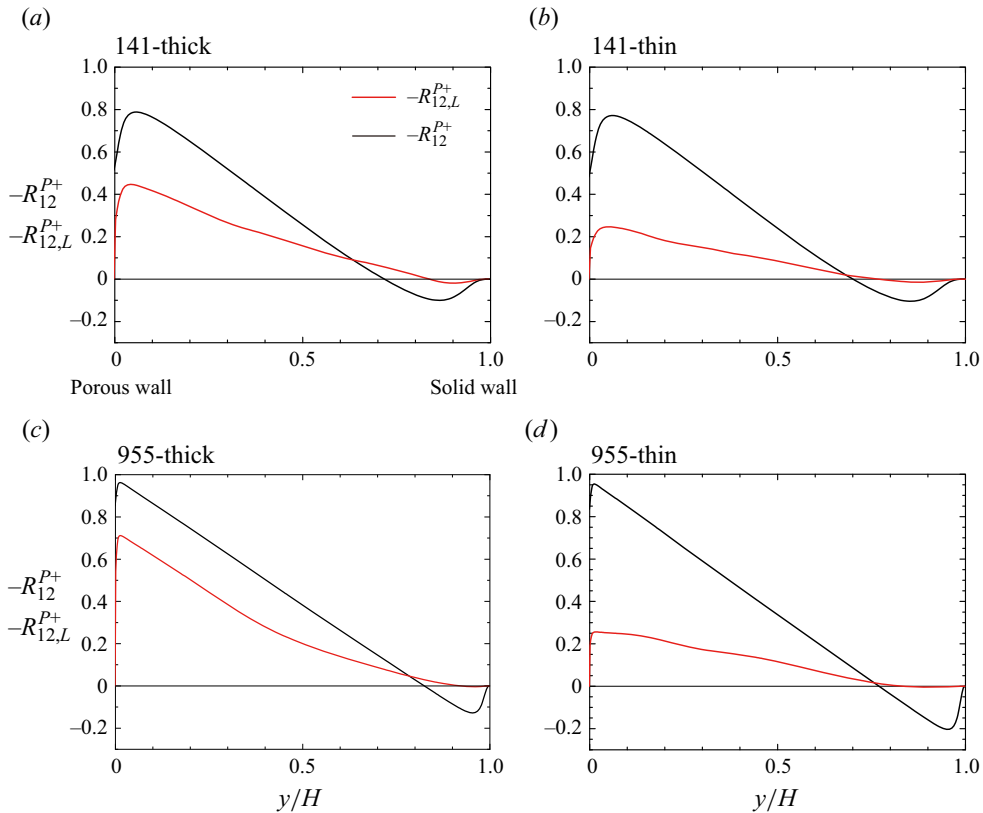
981 A3-12

Figure 7. Contributions of the decomposed Reynolds shear stress normalized by u_τ^p: (*a*) case 141-thick, (*b*) case 141-thin, (*c*) case 955-thick, and (*d*) case 955-thin. The Reynolds shear stress is denoted by R_{12}, and $R_{12,L}$ is the contribution by relatively large-scale velocity fluctuations defined as (3.1).

$R_{cor} = -R_{12}/(\sqrt{R_{11}}\sqrt{R_{22}})$. The dispersive covariance $\mathcal{T}_{12}$ consists of the mean velocity dispersion, which results from the tortuous mean velocity caused by the obstruction of the Kelvin cell arrays. When attention is paid to $-\mathcal{T}_{12}^+$, figures 9(*a*,*c*) show that $-\mathcal{T}_{12}^+$ is produced slightly below the porous/fluid interface, although we observe no perceptible effects of wall thickness on $-\mathcal{T}_{12}^+$. In other words, spanwise rollers do not significantly alter the mean velocity distribution below the porous/fluid interface. Regarding $-R_{12}^+$, figures 9(*a*,*c*) show that in the clear flow region, $-R_{12}^+$ for the thick-wall case shifts upwards with respect to the thin-wall results, which is pronounced at $Re_\tau = 955$ in figure 9(*c*). As the Reynolds shear stress dominates the momentum transfer, C_f^p in table 2 reflects the trend of $-R_{12}^+$; C_f^p for case 955-thick is 67 % larger than that for case 955-thin, whereas the increase ratio for case 141-thick is reduced to 20 %. Interestingly, near the porous/fluid interface ($-0.3 < y/H < 0.3$), the increased $-R_{12}^+$ for case 955-thick can be attributed to the increased correlation coefficient R_{cor} as shown in figure 9(*b*), which is most likely a sign of a more organized turbulence structure over the thick wall for case 955-thick. Above this region ($0.3 < y/H < 0.7$), the thickening of the wall does not increase R_{cor} but increases R_{11}^+ or R_{22}^+, as shown in figure 8(*d*), suggesting that the enhanced turbulence intensity contributes to an increase in $-R_{12}^+$ in this region. The same but less distinct trend is observed for case 141-thick in figure 9(*b*). Therefore, it is suggested that the increased
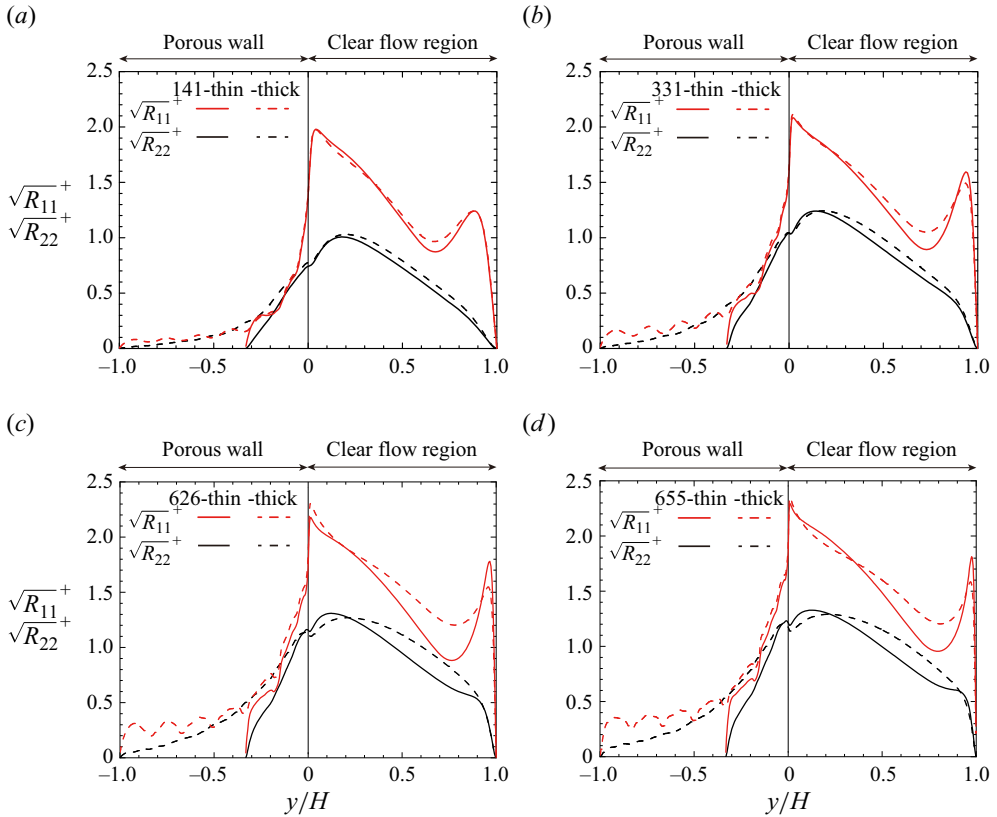
Figure 8. Streamwise and wall-normal turbulence intensities: (*a*) $Re_\tau = 141$, (*b*) $Re_\tau = 331$, (*c*) $Re_\tau = 626$, and (*d*) $Re_\tau = 955$.

C_f^p for the thick-wall cases, which is a result of the increased $-R_{12}^+$, is attributed to the combined effects of the enhanced turbulence intensity and organization.

To gain a better physical understanding of the modification of the correlation coefficient R_{cor}, the joint probability density function (JPDF) of streamwise and wall-normal velocity fluctuations at $y^{p+} \simeq 10$ for cases 955-thick and 955-thin is presented in figure 10. As interest is centred on the effects of spanwise rollers, the JPDF of the low-pass filtered velocity fluctuations with cutoff wavenumber $\kappa_x^* = \kappa_z^* = 2/(3H)$ is also presented in figures 10(*b,d*). Here, the cutoff wavenumber was the same as that used in the earlier analysis of the Reynolds shear stress decomposition in figure 7. We confirm from figures 10(*a,c*) that the JPDF is characterized by the intense sweep motion ($u' > 0$, $v' < 0$) and weak ejection motion ($u' < 0$, $v' > 0$). Attenuated wall-blocking effects result in an intense sweep towards the permeable porous wall, which pushes a high-momentum fluid into the porous wall leading to a seepage upward flow with a low-momentum fluid, that is, weak ejection. From figures 10(*a,c*), no major difference is observed between the P_{uv} for the thick- and thin-wall cases. However, for case 955-thick, intense sweep and weak ejection events occurred a little more frequently, and the JPDFs for inward ($u' < 0$, $v' < 0$) and outward ($u' > 0$, $v' > 0$) interaction events appear to shrink. Consequently, the correlation coefficient between u' and v' is 11 % larger for case 955-thick. Interestingly, the effect of wall thickness is magnified for the JPDF of the low-pass filtered velocities $P_{\hat{u}\hat{v}}$, as shown in figures 10(*b,d*). The probability density of the low-pass filtered velocities for
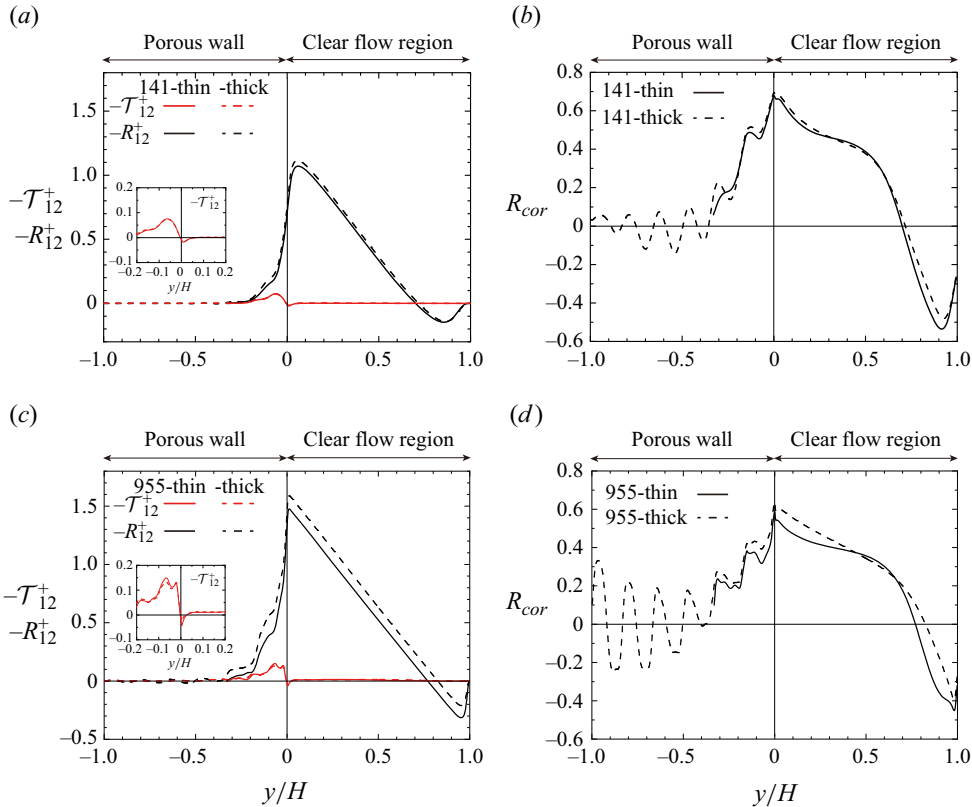
Figure 9. (*a*,*c*) Shear stress due to the turbulent velocity fluctuations, i.e. the Reynolds shear stress $R_{12} = \langle \overline{u'v'} \rangle$, and shear stress due to the tortuous mean velocity, i.e. the dispersive covariance $\mathcal{T}_{12} = \langle \tilde{\bar{u}} \, \tilde{\bar{v}} \rangle$. (*b*,*d*) Correlation coefficient for the Reynolds shear stress $R_{cor} = -R_{12}/(\sqrt{R_{11}}\sqrt{R_{22}})$. Plots for (*a*,*b*) $Re_\tau = 141$, and (*c*,*d*) $Re_\tau = 955$.

case 955-thin in figure 10(*b*) is clustered near the origin. In contrast, for case 955-thick in figure 10(*d*), the peak value of $P_{\hat{u}\hat{v}}$ decreases substantially, and the tails of $P_{\hat{u}\hat{v}}$ for the sweep and ejection events are stretched, indicating that the intense sweep and ejection events occur more frequently. Moreover, the negative correlation between $\widehat{u'}$ and $\widehat{v'}$ is more significant than that for the unfiltered velocity fluctuations. Given that low-pass filtered velocity fluctuations most likely result from spanwise rollers, as argued previously, it is conjectured that the increase in R_{cor} for case 955-thick is attributed to highly correlated large-scale velocity fluctuations, which are enhanced considerably by spanwise rollers.

These results indicate that two potential mechanisms may be involved in the increased friction coefficient by spanwise rollers. The first is the reinforcement of the negative correlation between the wall-normal and streamwise velocity fluctuations close to the porous/fluid interface. The second is the enhanced wall-normal and streamwise velocity fluctuations away from the porous/fluid interface. Both reinforce the Reynolds shear stress above the porous/fluid interface, resulting in an augmentation of momentum transfer.

3.4. *Logarithmic mean velocity profile*

This subsection explores the effects of spanwise rollers on the mean velocity profiles. For permeable or rough wall turbulence, the modified log law in (1.1) is used to characterize
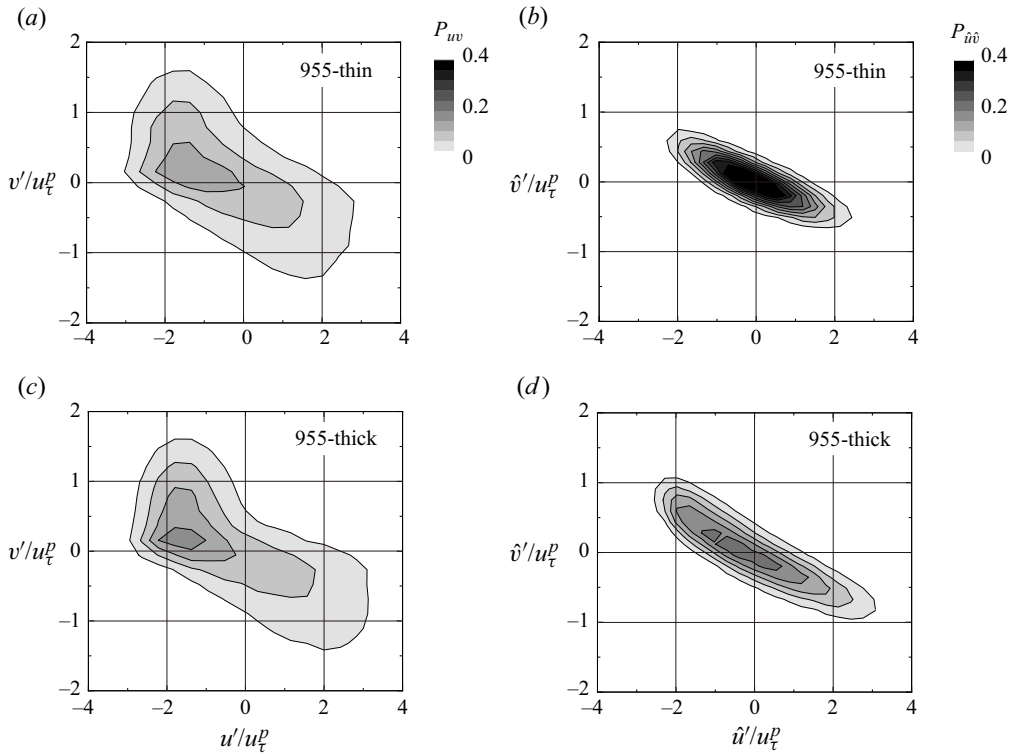
Figure 10. Joint probability density function (JPDF) of velocity fluctuations at $y^{p+} \simeq 10$: (*a,c*) JPDF of velocity fluctuations P_{uv}; (*b,d*) JPDF of low-pass filtered velocity fluctuations $P_{\hat{u}\hat{v}}$. Plots for (*a,b*) case 955-thin, and (*c,d*) case 955-thick.

the streamwise mean velocity profile. A common issue in permeable wall turbulence studies is how we parametrize the log-law parameters κ, d_p and h_r. Several approaches have been proposed and tested to determine the log-law parameters. Esteban *et al.* (2022) determined those parameters with an assumption that κ for the permeable wall turbulence is the same as that for smooth-wall turbulent boundary layers, κ_0, whereas Breugem *et al.* (2006), Suga *et al.* (2010) and Manes *et al.* (2011) determined the d_p value that forces $\gamma = (y + d_p)(dU^{p+}/dy)$ to be constant in the logarithmic region, which yields a κ value smaller than κ_0. Alternatively, Kuwata (2022*b*) determined the d_p value based on the Jackson model (Jackson 1981) and determined the value of κ using the profile of the diagnostic function γ, which on the contrary yielded a κ value larger than κ_0. The controversy regarding the κ value resides in the fact that there are several possible sets of parameters for plausibly approximating the mean velocity profiles over porous walls because of the presence of three free parameters: κ, d_p and h_r. However, as κ is linked originally to Prandtl's mixing-length hypothesis, κ is no longer a free parameter; instead, a physically appropriate value should be prescribed for κ. In this study, we do not resort to $\kappa = \kappa_0$ because spanwise rollers alter the turbulence statistics far from the porous/fluid interface, as discussed in the previous subsection, which possibly modifies the κ value. In addition, as the Reynolds number under consideration is not sufficiently high to perfectly guarantee a logarithmic mean velocity profile (Jiménez & Moser 2007; Lee & Moser 2015), we do not rely on the assumption of constant γ in the logarithmic region. Therefore, we follow the previous work of Kuwata (2022*b*), who did not assume γ to be constant, and

did not rely on $\kappa = \kappa_0$. This approach determines d_p using the extended Jackson model for pressure-driven turbulence boundary layers proposed by Breugem *et al.* (2006), where d_p is defined as the level at which the mean drag minus the mean pressure gradient acts as follows:

$$d_p = \frac{\displaystyle\int_{-h}^{0} y f_x \, \mathrm{d}y}{\displaystyle\int_{-h}^{0} f_x \, \mathrm{d}y}, \tag{3.2}$$

where f_x denotes the x–z plane averaged streamwise drag force exerted by the porous wall minus the mean pressure gradient (Breugem *et al.* 2006; Kuwata 2022*b*). The drag force includes the viscous and pressure drag forces, and plays a crucial role in the momentum transfer within the porous wall, which appears in the x–z plane averaged momentum equations.

To determine the von Kármán constant κ using the diagnostic function $\gamma = (y + d_p)(\mathrm{d}U^{p+}/\mathrm{d}y)$, figure 11 depicts the profiles of γ for the thin- and thick-wall cases. For comparison, the smooth-wall results at comparable friction Reynolds numbers 150 and 300 from Iwamoto *et al.* (2002), 590 from Vreman & Kuerten (2014), and 944 from Hoyas & Jiménez (2008), are shown. As is evident from the smooth-wall results shown in figure 11, the profiles do not exhibit a plateau value of γ owing to the low Reynolds number effects. Thus a logarithmic region cannot be rigorously expected for the present results. Nevertheless, the results have interesting implications regarding the slope of the logarithmic mean velocity. The first notable observation is that in the middle of the boundary layer, the γ profiles for the thin-wall cases collapse reasonably onto the smooth-wall results, except for the lowest Re_τ cases in figure 11(*a*). This suggests that the slope of the mean velocity profile is not altered by the thin wall. Similar observations were made for rough wall turbulence (Jiménez 2004), and this may substantiate the outer layer similarity, in which the wall roughness retards the mean velocity, yet is not felt by the turbulence far from rough walls (Townsend 1980). Thus, in this sense, the present thin porous wall behaves more like a rough wall than a permeable wall. Note that the small discrepancy with the smooth-wall results is due to the large size of the Kelvin cell and the small Re_τ because the similarity hypothesis holds only if the roughness elements are sufficiently small and the Reynolds number is sufficiently high. The reasonable agreement of γ with the smooth-wall results implies that the thin wall does not change κ from the smooth-wall value κ_0; that is, $\kappa \simeq \kappa_0$.

In contrast, γ for the thick-wall cases largely deviates from the smooth-wall results. Interestingly, figures 11(*b*–*d*) confirm that γ is shifted downwards with respect to the smooth-wall results. Given that γ in the logarithmic region is related to the inverse of κ, the introduction of the downward shift $\Delta\gamma$, i.e. $1/\kappa = 1/\kappa_0 + \Delta\gamma$, may modify the von Kármán constant as follows:

$$\kappa = \frac{\kappa_0}{1 - \kappa_0 \, \Delta\gamma}. \tag{3.3}$$

Evidently, the positive value of $\Delta\gamma$ yields a larger κ value compared with the smooth-wall value κ_0. A physical explanation for the increase in κ can be provided based on the classical mixing length model. The modelled Reynolds shear stress based on the concept of mixing length hypothesis is expressed as

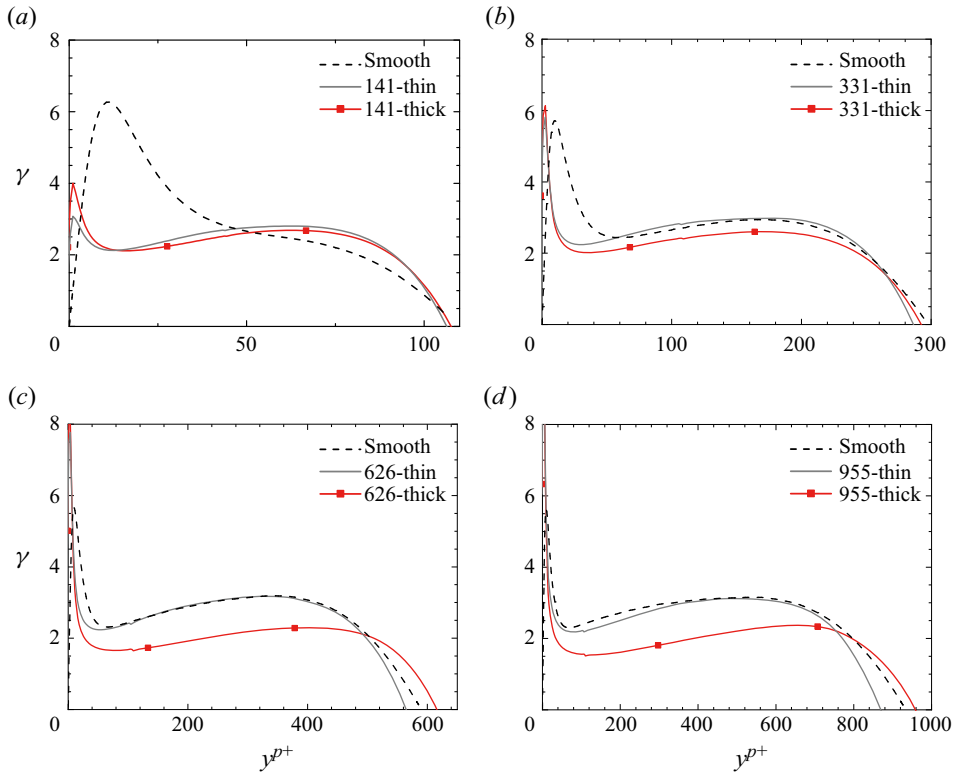$$-R_{12} = -\ell_M^2 \left| \frac{\mathrm{d}U}{\mathrm{d}y} \right| \frac{\mathrm{d}U}{\mathrm{d}y}, \tag{3.4}$$

981 A3-17

Figure 11. Comparison of the diagnostic function $\gamma = (y + d_p)(\mathrm{d}U^{p+}/\mathrm{d}y)$: (*a*) $Re_\tau = 141$, (*b*) $Re_\tau = 331$, (*c*) $Re_\tau = 626$, and (*d*) $Re_\tau = 955$. For comparison, we include the smooth-wall results at $Re_\tau = 150$ from Iwamoto, Suzuki & Kasagi (2002) in (*a*), $Re_\tau = 300$ from Iwamoto *et al.* (2002) in (*b*), $Re_\tau = 590$ from Vreman & Kuerten (2014) in (*c*), and $Re_\tau = 944$ from Hoyas & Jiménez (2008) in (*d*).

where ℓ_M denotes the mixing length. For the thick-wall cases, where the effects of the K–H instability emerge, figure 7 shows that the Reynolds shear stress is caused primarily by relatively large-scale velocity fluctuations induced by spanwise rollers. Hence the mixing length, which is related to the turbulent vortex scale, can presumably be increased by spanwise rollers. This idea is consistent with that mentioned by Poggi *et al.* (2004), who discussed the modelling of vegetation canopy turbulence based on an increased mixing length. Assuming that the inner-scaled total stress, which consists of viscous and turbulent stresses, is unity in the inner layer, the mean velocity gradient is expressed in terms of the mixing length, as

$$\frac{\mathrm{d}U^{p+}}{\mathrm{d}y^{p+}} = \frac{2}{1 + \sqrt{1 + 4(\ell_M^{p+})^2}}. \tag{3.5}$$

This equation indicates that an increased mixing length leads to a decrease in the mean velocity gradient and the diagnostic function $\gamma = (y + d_p)(\mathrm{d}U^{p+}/\mathrm{d}y)$, resulting in an increase in the von Kármán constant κ through the relationship $\kappa = \gamma^{-1}$. Therefore, it can be argued that the emergence of the effects of the K–H instability is the main cause of the increase in κ. Once κ and d_p are known, the h_r value is obtained by collapsing the mean velocity profile into the modified log law. These parameters are summarized

in figure 12, where parameters κ, d_p^{p+} and h_r^{p+} are plotted against $Re_K = \sqrt{K}^{p+}$. Here, $\kappa_0 = 0.4$ is used as the smooth-wall value; thus κ for the thin-wall cases is assumed to be $\kappa = \kappa_0 = 0.4$. For the lowest Re_τ cases, we assume that κ for case 141-thin remains unchanged from the smooth-wall value, as in the other thin-wall cases, whereas κ for case 141-thick is estimated from the downshift value of γ with respect to the thin-wall result from figure 11(*a*). The surrogate κ values and the resulting h_r^{p+} values are denoted by the open symbols in the figure. Figures 12(*a,b*) show that d_p^{p+} and h_r^{p+} are proportional to Re_K except for h_r^{p+} at $Re_\tau = 141$ (cases 141-thick and 141-thin), indicating that $d_p \propto \sqrt{K}$ and $h_r \propto \sqrt{K}$. This means that parameters d_p and h_r are connected to a physical length scale, even though these parameters are flow properties. This supports the findings of previous experiments on turbulent flows over porous foams by Manes *et al.* (2011) and Suga *et al.* (2010), although the proportionality constants of these studies disagree with the present results because of the differences in the procedures for obtaining d_p and h_r. Regarding the von Kármán constant κ in figure 12(*c*), κ for the thick-wall cases increases with Re_K and become saturated to $\kappa \simeq 0.6$ at $Re_K > 30$. This reflects the dominance of spanwise rollers, as shown in figure 5; the effect of the K–H instability is weak for case 141-thick, but increases with the Reynolds number. The κ value increases correspondingly, although eventually, κ reaches a plateau in the 'ultimate porous wall turbulence regime' for cases 626-thick and 955-thick where the dominance of velocity fluctuations associated with the K–H instability is almost unaffected by the Reynolds number. The inner-scaled mean velocity profiles along with the resulting log-law profiles are shown in figure 13. For comparison, the smooth-wall results at $Re_\tau = 944$ from Hoyas & Jiménez (2008), and $Re_\tau = 109$ from Iwamoto *et al.* (2002), are included. For the porous wall side, the figure confirms that U^{p+} profiles over the porous walls can be approximated reasonably using the modified log law of (1.1). The slope of the U^{p+} profile for the thick-wall cases in figure 13(*a*) decreases with Re_τ, whereas the slope does not change for thin-wall cases in figure 13(*b*). For thin-wall cases, as the slopes of the U^{p+} profiles are unchanged and $d_p \propto \sqrt{K}$, the U^{p+} profiles can be expressed as smooth-wall profiles with a downward shift of ΔU^{p+}. This downward shift is referred to as roughness function ΔU^{p+} and is expressed in terms of h_r as

$$\Delta U^{p+} = \frac{1}{\kappa} \ln(h_r^{p+}) + B, \qquad (3.6)$$

where B is the log-law intercept for smooth-wall turbulence. Using the earlier observation of $h_r \propto \sqrt{K}$, we can cast (3.6) into the correlation for ΔU^{p+} in the fully rough regime (Flack & Schultz 2010):

$$\Delta U^{p+} = \frac{1}{\kappa} \ln(k_s^{p+}) + B - 8.5, \qquad (3.7)$$

where the equivalent sand grain roughness can be related to $k_s = h_r \exp(8.5\kappa)$. The earlier observation of $h_r \propto \sqrt{K}$ leads to $k_s \propto \sqrt{K}$, suggesting that the equivalent sand grain roughness is related to the square root of the permeability. The thin porous walls in the present study yields $k_s \simeq 13\sqrt{K}$, although the proportional constant may depend on the geometry of the porous walls. Hence, the earlier observations of $\kappa = \kappa_0$, $h_r \propto \sqrt{K}$ and $d_p \propto \sqrt{K}$ suggest that the mean velocity profiles over thin walls can be expressed similarly to the rough wall turbulence in the fully rough regime, where the roughness is no longer within the viscous sublayer but protrudes into the logarithmic region. Judging
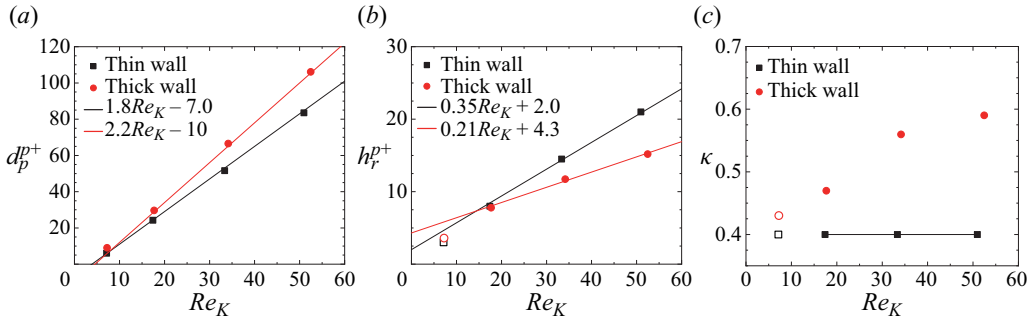
(*a*)   (*b*)   (*c*)

Figure 12. Parameters for modified log law versus the permeability Reynolds number Re_K: (*a*) zero-plane displacement d_p^{p+}, (*b*) equivalent roughness height h_r^{p+}, and (*c*) von Kármán constant κ. Open symbols denote the surrogate values for the lowest Re_τ cases. The linear fitted lines are added in (*a,b*).

from the roughness Reynolds number for case 141-thin of $k_s^+ \simeq 90$, the turbulent flow for case 141-thin may not be perfectly within the fully rough regime, although the onset of the fully rough regime remains controversial (Flack, Schultz & Rose 2012). This is the reason why $h_r \propto \sqrt{K}$ is not retained for case 141-thin. In contrast, for thick-wall cases, the thick walls allow for the development of spanwise rollers, leading to an increased κ. This makes it impossible to use the concept of the roughness function ΔU^{p+} because the slopes of the U^{p+} profiles over the thick walls are no longer the same as those of the smooth-wall profiles. Moreover, there may be an interaction between roughness-induced turbulent vortices and spanwise rollers. Therefore, the equivalent roughness height h_r for the thick-wall cases differs from the corresponding values for the thin-wall cases as shown in figure 12, despite the fact the geometry of the subsurface porous wall remains the same. Interestingly, the effects of the wall thickness are also visible for the U^{s+} profile for the smooth-wall side. We observe that the U^{s+} profile tends to be lower for the thick-wall cases. The U^{s+} profiles for cases 626-thin and 955-thin in figure 13(*b*) are close to the DNS results at $Re_\tau = 109$, whereas the corresponding profiles for the thick-wall cases in figure 13(*a*) are below the DNS profiles. This is reflected in the skin friction coefficient, as shown in figure 3, which shows that the thickening of the wall increases C_f^s. Although the mechanisms are not clear, it is evident that spanwise rollers, which develop over thick walls, affect the turbulence for the other side of the smooth wall.

3.5. *Predictive model for the skin friction coefficient*

The log-law parameters d_p, h_r and κ are crucial for predicting mean flows over porous walls. Hence, in this subsection, we discuss predictive models for these parameters, with the aid of the earlier findings for $\kappa \neq \kappa_0$, $h_r \propto \sqrt{K}$ and $d_p \propto \sqrt{K}$ for thick walls. To develop widely applicable models, the validity of the developed model for a variety of porous media must be assessed. However, a direct comparison of the log-law parameters in the literature is meaningless because these parameters depend strongly on the determination procedure. Alternatively, we assess C_f^p predicted by the modified log law using the modelled log-law parameters, which enables us to briefly assess the validity of the developed models of d_p, h_r and κ for large amounts of experimental and DNS data. Assuming a flow with a high Reynolds number where a large portion of the clear flow region is occupied by the logarithmic region, the bulk mean velocity U_b^{p+} can be
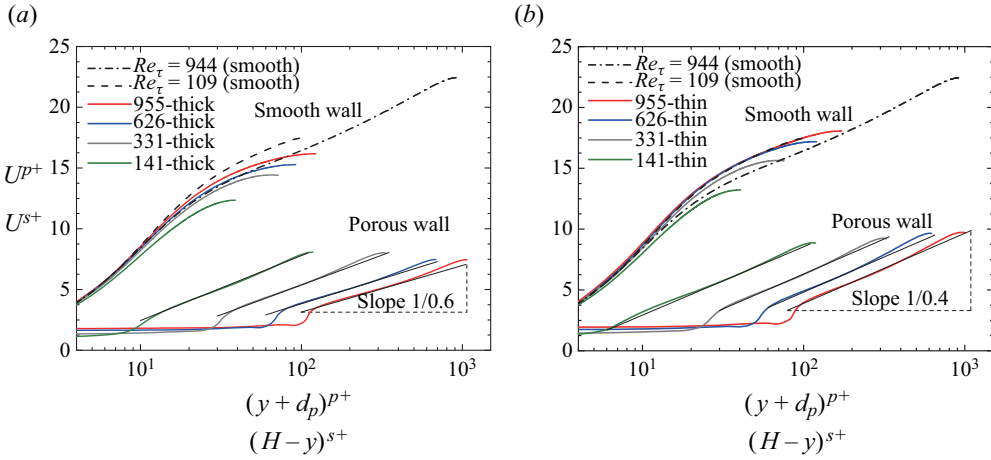
981 A3-20

Figure 13. Inner-scaled mean velocity profiles for the porous wall side U^{p+} and smooth-wall side U^{s+}: (*a*) thick-wall cases, and (*b*) thin-wall cases. The mean velocity U^{p+} is plotted against $(y + d_p)^{p+}$, while U^{s+} is plotted against the distance from the smooth wall $(H - y)^{s+}$. For comparison, the smooth-wall results at $Re_\tau = 944$ from Hoyas & Jiménez (2008), and $Re_\tau = 109$ from Iwamoto *et al.* (2002), are included. The thin solid lines denote the modified log-law profiles with the log-law parameters in figure 12.

approximated by integrating the modified log law:

$$U_b^{p+} \simeq \frac{1}{\delta_p} \int_0^{\delta_p} \frac{1}{\kappa} \ln\left(\frac{y + d_p}{h_r}\right) \mathrm{d}y = \frac{1}{\kappa}\left[\ln\left(\frac{\delta_p + d_p}{h_r}\right) + \frac{d_p}{\delta_p}\ln\left(\frac{\delta_p + d_p}{d_p}\right) - 1\right]. \quad (3.8)$$

This yields the skin friction coefficient $C_f^p = 2/(U_b^{p+})^2$:

$$C_f^p = 2\kappa^2\left[\ln\left(\frac{\delta_p + d_p}{h_r}\right) + \frac{d_p}{\delta_p}\ln\left(\frac{\delta_p + d_p}{d_p}\right) - 1\right]^{-2}. \quad (3.9)$$

An important implication of (3.9) is that for high Reynolds number flows over a porous wall where we assume $\kappa = \mathrm{const.}$, $d_p \propto \sqrt{K}$ and $h_r \propto \sqrt{K}$, the skin friction coefficient depends on the square root of the Darcy number, $\sqrt{Da} = \sqrt{K}/\delta_p$, but does not depend on the Reynolds number:

$$C_f^p = 2\kappa^2\left[\ln\left(\frac{1 + C_1\sqrt{Da}}{C_2\sqrt{Da}}\right) + C_1\sqrt{Da}\ln\left(\frac{1 + C_1\sqrt{Da}}{C_1\sqrt{Da}}\right) - 1\right]^{-2}, \quad (3.10)$$

where C_1 and C_2 are the proportionality constants for d_p and h_r with $\sqrt{K}$, respectively. The Reynolds number independence of C_f^p is consistent with observations in experimental (Suga *et al.* 2010; Esteban *et al.* 2022) and DNS (Motoki *et al.* 2022) studies.

For the present porous wall (thick-wall cases), we obtain a set of correlations of the log-law parameters in the 'ultimate porous wall turbulence regime' as shown in figure 12:

$$\left.\begin{aligned}
\kappa &= 0.6, \\
d_p^{p+} &= 2.2\,Re_K - 10, \\
h_r^{p+} &= 0.21\,Re_K + 4.3.
\end{aligned}\right\} \quad (3.11)$$

For low Re_K flows ($Re_K < 30$), h_r^{p+} is lower than the linear correlation in (3.11), and κ approaches the smooth-wall value asymptotically. To reproduce a low Re_K limit where
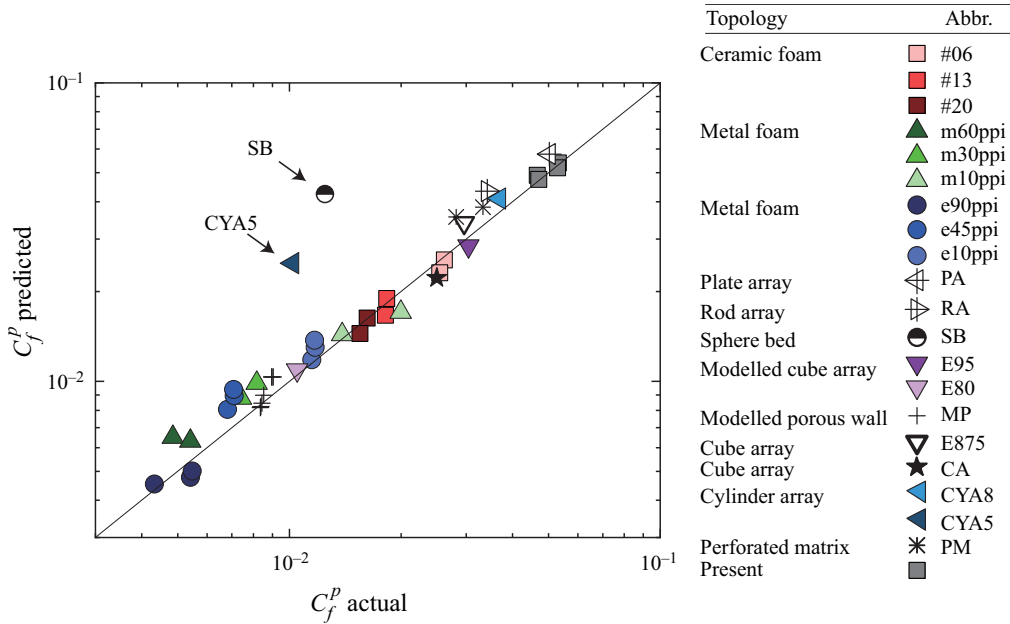
Figure 14. Comparison of the predicted and actual C_f^p. The predicted C_f^p is given by (3.9) with (3.12) and (3.13). For reference data, we include the experimental data for ceramic foam (Suga *et al.* 2010), metal foam (Manes *et al.* 2011; Esteban *et al.* 2022), packed beds of spheres (Manes *et al.* 2009), rod array (Dunn, López & García 1996) and plate array (Nezu & Sanjou 2008). Moreover, we include the DNS data for a modelled cube array (Breugem *et al.* 2006), modelled porous wall (Rosti, Cortelezzi & Quadrio 2015), cube arrays (Breugem & Boersma 2005; Kuwata & Suga 2016*b*), cylinder array (Chu *et al.* 2021) and perforated matrix (Kuwata & Suga 2017). The thin line denotes that the predicted C_f^p is equal to the actual C_f^p.

the modified log law returns to the standard log law, that is, $\kappa = \kappa_0$, $d_p^{p+} = 0$ and $h_r^{p+} = \exp(-B\kappa)$, we introduced damping functions to correct the limiting behaviour of the set of correlations:

$$\left.\begin{array}{c} \kappa = 0.6f_1 + \kappa_0(1 - f_1), \\ d_p^{p+} = \max(2.2\,Re_K - 10, 0), \\ h_r^{p+} = (0.21\,Re_K + 4.3)f_2 + \exp(-B\kappa)(1 - f_2). \end{array}\right\} \quad (3.12)$$

Here, we employ simple expressions for the damping functions f_1 and f_2:

$$\left.\begin{array}{c} f_1 = 1 - \exp(-Re_K^{1.5}/164), \\ f_2 = 1 - \exp(-Re_K^{1.5}/22.6), \end{array}\right\} \quad (3.13)$$

where the damping functions are tuned based on the present DNS results for the thick-wall cases. To test the applicability of the models, C_f^p predicted by (3.9) with a set of modelled correlations was compared with the available experimental and DNS results. The results are shown in figure 14, which includes 38 reference data for 20 porous media, including experimental data for ceramic foams (Suga *et al.* 2010), metal foams (Manes *et al.* 2011; Esteban *et al.* 2022), packed beds of spheres (Manes *et al.* 2009), rod array (Dunn *et al.* 1996) and plate array (Nezu & Sanjou 2008), and the DNS data for the cube arrays (Breugem & Boersma 2005; Kuwata & Suga 2016*b*), cylinder arrays (Chu *et al.* 2021)

Reference	Topology	Abbr.	Method	φ	Re_K
Suga *et al.* (2010)	Ceramic foam	#06	Exp.	0.80	6.2–11.1
		#13		0.81	3.2–6.1
		#20		0.82	2.4–4.5
Manes *et al.* (2011)	Metal foam	m60ppi	Exp.	0.98	1.9–2.2
		m30ppi		0.97	3.2–7.9
		m10ppi		0.96	8.4–17.2
Esteban *et al.* (2022)	Metal foam	e90ppi	Exp.	0.96	1.6–4.7
		e45ppi		0.97	7.3–19.5
		e10ppi		0.98	24.9–63.2
Manes *et al.* (2009)	Sphere bed	SB	Exp.	0.48	44.6
Dunn *et al.* (1996)	Rod array	RA	Exp.	0.99	1497
Nezu & Sanjou (2008)	Plate array	PA	Exp.	0.99	134
Breugem *et al.* (2006)	Modelled cube array	E95	DNS	0.95	9.4
		E80		0.80	1.1
Rosti *et al.* (2015)	Modelled porous wall	MP	DNS	0.6	0.045–0.75
				0.9	0.75
Breugem & Boersma (2005)	Cube array	E875	DNS	0.875	12.3
Kuwata & Suga (2016*b*)	Cube array	CA	DNS	0.71	3.8
Chu *et al.* (2021)	Cylinder array	CY8	DNS	0.8	32.3
		CY5		0.5	9.3
Kuwata & Suga (2017)	Perforated matrix	PM	DNS	0.84	6.1
				0.84	13.1

Table 3. Characteristics of the tested porous media.

and perforated matrix (Kuwata & Suga 2017). We also include the DNS data based on the volume-averaged Navier–Stokes equations (Breugem *et al.* 2006; Rosti *et al.* 2015). The porosity φ and permeability Reynolds number Re_K of the tested porous media are summarized in table 3. As shown in table 3, except for the packed beds of spheres (SB) and cylinder arrays (CYA5), the tested porous media have a relatively high porosity value ($\varphi \geq 0.6$), and the permeability Reynolds number Re_K ranges from 1.1 to 1500. For the cylinder arrays (CYA5 and CYA8) from Chu *et al.* (2021), we prescribed the permeability using the empirical correlation proposed by Macdonald *et al.* (1979). For the rod array (Dunn *et al.* 1996) and plate array (Nezu & Sanjou 2008), we used the permeability values given by Kuwata & Suga (2015). The skin friction coefficient over the metal foam in Esteban *et al.* (2022) was defined based on the free-stream velocity. Accordingly, for these cases, we alternatively define C_f^p based on the mean velocity at the edge of the boundary layer $y = \delta_p$ as

$$C_f^p = 2\kappa^2 \left[\ln \left(\frac{\delta_p + d_p}{h_r} \right) \right]^{-2}. \tag{3.14}$$

The figure shows that the predicted C_f^p correlates well with the actual C_f^p value, although the proposed model considerably overestimates C_f^p for cases CYA5 and SB, where the porosity values are relatively low. This demonstrates the validity of the proposed model for various porous media with high porosity, despite the fact that the proposed model was optimized using only the present DNS data. It can be interpreted that the wall permeability is a key parameter that characterizes the logarithmic mean velocity profiles over various porous media as long as the porous media have a high porosity ($\varphi \geq 0.6$).

A plausible explanation for the overestimation of the low-porosity cases is that the proposed model fails to account for inertial drag effects. The drag force acting on the porous medium F_x can be modelled as a combination of linear and quadratic terms with respect to the velocity, and is given by the Darcy–Forchheimer equation (Whitaker 1996)

$$F_x = \nu K^{-1} U_d + c_F K^{-1/2} U_d \sqrt{U_d^2}, \tag{3.15}$$

where c_F denotes the Forchheimer coefficient. It is evident from the Darcy–Forchheimer equation (3.15) that the coefficient of the inertia term depends on K and c_F. Hence both K and c_F are essential to account correctly for the effects of porous wall-induced drag. However, the present model does not include c_F, which drastically increases with decreasing porosity (Ergun 1952; Macdonald *et al.* 1979). Therefore, further correction using c_F may be required to extend the model to low-porosity porous media, such as gravel beds and packed spheres. Regarding the effects of porosity φ, it is worth noting that the DNS study for the modelled low-permeable wall by Rosti *et al.* (2015) demonstrated that the effects of φ and K are quite different; φ has little effect on the turbulence statistics, whereas the turbulence is affected strongly by K. This may be supported by the previous DNS study by Breugem *et al.* (2006), which showed that the φ gradient terms in the spatial and Reynolds-averaged momentum equations do not contribute significantly to the momentum transfer. However, because the coefficients of the Darcy–Forchheimer equation, i.e. K and c_F, are related to φ (Ergun 1952; Macdonald *et al.* 1979), indirectly a decrease in φ attenuates the turbulence enhancement effect (Breugem & Boersma 2005; Chu *et al.* 2021) via a decrease in K and an increase in c_F.

4. Conclusions

The effects of Reynolds number on permeable porous wall turbulence were studied by performing DNS of turbulent flows over a highly permeable porous medium at different friction Reynolds numbers. The porous wall comprised Kelvin cell arrays with porosity 0.95, and the permeability Reynolds number ranged from $Re_K \simeq 7$ to $Re_K \simeq 50$. For the porous walls, thin and thick porous substrates were studied to identify the effects of spanwise rollers associated with the Kelvin–Helmholtz (K–H) instability. We found that the effect of the K–H instability emerges for the thick porous wall; the effect of the K–H instability is more pronounced with increasing Reynolds number, and spanwise roller vortices dominate turbulence in the clear flow region when $Re_K \gtrsim 30$. Spanwise rollers reinforce the negative correlation between the wall-normal and streamwise velocity fluctuations close to the porous/fluid interface, and intensify the turbulent velocity fluctuations away from the porous walls, resulting in increased frictional resistance through Reynolds shear stress enhancement over the porous walls. Hence the augmentation of frictional resistance becomes more significant with increasing Reynolds number, corresponding to the dominance of the velocity fluctuations associated with the K–H instability. Once turbulence is dominated by channel height scale spanwise rollers, which is referred to as the 'ultimate porous wall turbulence regime' in this study, the turbulence structure and skin friction coefficient are almost unaffected by the Reynolds number.

An investigation of the Reynolds number dependence of the modified log law reveals that the zero-plane displacement and equivalent roughness height are proportional to the length scale of the porous media, regardless of the wall thickness, whereas spanwise rollers increase the von Kármán constant. For thick porous walls, the zero-plane displacement and equivalent roughness height are modelled as linear functions of the square root

of the permeability. Spanwise rollers over thick porous walls increase the von Kármán constant as the Reynolds number increases, and become saturated to $\kappa \simeq 0.6$ in the 'ultimate porous wall turbulence regime' at $Re_K > 30$. The proposed model based on permeability is validated by comparing the skin friction coefficient obtained from the modified log law with the available DNS and experimental data. The proposed model reasonably predicts the skin friction coefficient for several types of porous media with high porosity. Hence, permeability is regarded as a key parameter that characterizes the logarithmic mean velocity profiles over various porous media with high porosity ($\varphi \geq 0.6$), although further correction using the porosity or Forchheimer coefficient may be required to extend this model to low-porosity porous media.

Declaration of interests. The authors report no conflict of interest.

Author ORCIDs.

Y. Kuwata https://orcid.org/0000-0002-9489-2788;

K. Suga https://orcid.org/0000-0001-9313-1816.

REFERENCES

BREUGEM, W.P. & BOERSMA, B.J. 2005 Direct numerical simulations of turbulent flow over a permeable wall using a direct and a continuum approach. *Phys. Fluids* **17** (2), 025103.

BREUGEM, W.P., BOERSMA, B.J. & UITTENBOGAARD, R.E. 2006 The influence of wall permeability on turbulent channel flow. *J. Fluid Mech.* **562**, 35–72.

CHANDESRIS, M., D'HUEPPE, A., MATHIEU, B., JAMET, D. & GOYEAU, B. 2013 Direct numerical simulation of turbulent heat transfer in a fluid-porous domain. *Physic. Fluids* **25** (12), 125110.

CHU, X., WANG, W., YANG, G., TERZIS, A., HELMIG, R. & WEIGAND, B. 2021 Transport of turbulence across permeable interface in a turbulent channel flow: interface-resolved direct numerical simulation. *Trans. Porous Media* **136**, 165–189.

DETERT, M., NIKORA, V. & JIRKA, G.H. 2010 Synoptic velocity and pressure fields at the water–sediment interface of streambeds. *J. Fluid Mech.* **660**, 55–86.

DUNN, C., LÓPEZ, F. & GARCÍA, M. 1996 Mean flow and turbulence in a laboratory channel with simulated vegetation. *Tech. Rep.* 51. Dept. Civil Eng., University of Illinois Urbana-Champaign.

EFSTATHIOU, C. & LUHAR, M. 2018 Mean turbulence statistics in boundary layers over high-porosity foams. *J. Fluid Mech.* **841**, 351–379.

ENDRIKAT, S., MODESTI, D., GARCÍA-MAYORAL, R., HUTCHINS, N. & CHUNG, D. 2021 Influence of riblet shapes on the occurrence of Kelvin–Helmholtz rollers. *J. Fluid Mech.* **913**, A37.

ERGUN, S. 1952 Fluid flow through packed columns. *Chem. Engng Prog.* **48** (2), 89–94.

ESTEBAN, L.B., RODRÍGUEZ-LÓPEZ, E., FERREIRA, M.A. & GANAPATHISUBRAMANI, B. 2022 Mean flow of turbulent boundary layers over porous substrates. *Phys. Rev. Fluids* **7** (9), 094603.

FINNIGAN, J. 2000 Turbulence in plant canopies. *Annu. Rev. Fluid Mech.* **32** (1), 519–571.

FLACK, K.A. & SCHULTZ, M.P. 2010 Review of hydraulic roughness scales in the fully rough regime. *J. Fluids Engng* **132** (4), 041203.

FLACK, K.A., SCHULTZ, M.P. & ROSE, W.B. 2012 The onset of roughness effects in the transitionally rough regime. *Intl J. Heat Fluid Flow* **35**, 160–167.

GARCÍA-MAYORAL, R. & JIMÉNEZ, J. 2011 Drag reduction by riblets. *Phil. Trans. R. Soc.* A **369** (1940), 1412–1427.

GARCIA-MAYORAL, R. & JIMÉNEZ, J. 2012 Scaling of turbulent structures in riblet channels up to $Re_\tau \simeq$ 550. *Phys. Fluids* **24** (10), 105101.

GUAN, L., SALINAS, J.S., ZGHEIB, N. & BALACHANDAR, S. 2021 The role of bed-penetrating Kelvin–Helmholtz vortices on local and instantaneous bedload sediment transport. *J. Fluid Mech.* **911**, A50.

HO, R.T. & GELHAR, L.W. 1973 Turbulent flow with wavy permeable boundaries. *J. Fluid Mech.* **58**, 403–414.

HOYAS, S. & JIMÉNEZ, J. 2008 Reynolds number effects on the Reynolds-stress budgets in turbulent channels. *Phys. Fluids* **20** (10), 101511.

IWAMOTO, K., SUZUKI, Y. & KASAGI, N. 2002 Database of fully developed channel flow – THTLAB internal report. Rapport technique, THTLAB, Dept. of Mech. Engng., Univ. of Tokyo.

JACKSON, P.S. 1981 On the displacement height in the logarithmic velocity profile. *J. Fluid Mech.* **111**, 15–25.

JHA, N.K. & STEINBERG, V. 2021 Elastically driven Kelvin–Helmholtz-like instability in straight channel flow. *Proc. Natl Acad. Sci. USA* **118** (34), e2105211118.

JIMÉNEZ, J. 2004 Turbulent flows over rough walls. *Annu. Rev. Fluid Mech.* **36**, 173–196.

JIMÉNEZ, J. & MOSER, R.D. 2007 What are we learning from simulating wall turbulence? *Phil. Trans. R. Soc.* A **365** (1852), 715–732.

JIMÉNEZ, J., UHLMANN, M., PINELLI, A. & KAWAHARA, G. 2001 Turbulent shear flow over active and passive porous surfaces. *J. Fluid Mech.* **442**, 89–117.

KUWATA, Y. 2022*a* Dissimilar turbulent heat transfer enhancement by Kelvin–Helmholtz rollers over high-aspect-ratio longitudinal ribs. *J. Fluid Mech.* **952**, A21.

KUWATA, Y. 2022*b* Role of spanwise rollers by Kelvin–Helmholtz instability in turbulence over a permeable porous wall. *Phys. Rev. Fluids* **7** (8), 084606.

KUWATA, Y. & SUGA, K. 2015 Progress in the extension of a second-moment closure for turbulent environmental flows. *Intl J. Heat Fluid Flow* **51**, 268–284.

KUWATA, Y. & SUGA, K. 2016*a* Imbalance-correction grid-refinement method for lattice Boltzmann flow simulations. *J. Comput. Phys.* **311**, 348–362.

KUWATA, Y. & SUGA, K. 2016*b* Lattice Boltzmann direct numerical simulation of interface turbulence over porous and rough walls. *Intl J. Heat Fluid Flow* **61**, 145–157.

KUWATA, Y. & SUGA, K. 2017 Direct numerical simulation of turbulence over anisotropic porous media. *J. Fluid Mech.* **831**, 41–71.

KUWATA, Y. & SUGA, K. 2019 Extensive investigation of the influence of wall permeability on turbulence. *Intl J. Heat Fluid Flow* **80**, 108465.

KUWATA, Y., TSUDA, K. & SUGA, K. 2020 Direct numerical simulation of turbulent conjugate heat transfer in a porous-walled duct flow. *J. Fluid Mech.* **904**, A9.

LEE, M. & MOSER, R.D. 2015 Direct numerical simulation of turbulent channel flow up to $Re_\tau \approx 5200$. *J. Fluid Mech.* **774**, 395–415.

LOVERA, F. & KENNEDY, J.F. 1969 Friction factors for flat bed flows in sand channels. *J. Hydraul. Div. ASCE* **95**, 1227–1234.

MACDONALD, I.F., EL-SAYED, M.S., MOW, K. & DULLIEN, F.A.L. 1979 Flow through porous media – the Ergun equation revisited. *Ind. Engng Chem. Fundam.* **18** (3), 199–208.

MANES, C., POGGI, D. & RIDOL, L. 2011 Turbulent boundary layers over permeable walls: scaling and near-wall structure. *J. Fluid Mech.* **687**, 141–170.

MANES, C., POKRAJAC, D., MCEWAN, I. & NIKORA, V. 2009 Turbulence structure of open channel flows over permeable and impermeable beds: a comparative study. *Phys. Fluids* **21** (12), 125109.

MOTOKI, S., TSUGAWA, K., SHIMIZU, M. & KAWAHARA, G. 2022 The ultimate state of turbulent permeable-channel flow. *J. Fluid Mech.* **931**, R3.

NEPF, H. & GHISALBERTI, M. 2008 Flow and transport in channels with submerged vegetation. *Acta Geophys.* **56**, 753–777.

NEPF, H.M. & VIVONI, E.R. 2000 Flow structure in depth-limited, vegetated flow. *J. Geophys. Res.* **105** (C12), 28547–28557.

NEZU, I. & SANJOU, M. 2008 Turburence structure and coherent motion in vegetated canopy open-channel flows. *J. Hydro-Environ. Res.* **2**, 62–90.

NISHIYAMA, Y., KUWATA, Y. & SUGA, K. 2020 Direct numerical simulation of turbulent heat transfer over fully resolved anisotropic porous structures. *Int. J. Heat Fluid Flow* **81**, 108515.

POGGI, D., PORPORATO, A., RIDOLFI, L., ALBERTSON, J.D. & KATUL, G.G. 2004 The effect of vegetation density on canopy sub-layer turbulence. *Boundary-Layer Meteorol.* **111**, 565–587.

ROSTI, M.E. & BRANDT, L. 2017 Numerical simulation of turbulent channel flow over a viscous hyper-elastic wall. *J. Fluid Mech.* **830**, 708–735.

ROSTI, M.E., CORTELEZZI, L. & QUADRIO, M. 2015 Direct numerical simulation of turbulent channel flow over porous walls. *J. Fluid Mech.* **784**, 396–442.

ROY, A.G., BUFFIN-BELANGER, T., LAMARRE, H. & KIRKBRIDE, A.D. 2004 Size, shape and dynamics of large-scale turbulent flow structures in a gravel-bed river. *J. Fluid Mech.* **500**, 1–27.

STOESSER, T., BRAUN, C., GARCIA-VILLALBA, M. & RODI, W. 2008 Turbulence structures in flow over two-dimensional dunes. *J. Hydraul. Engng ASCE* **134** (1), 42–55.

SUGA, K., KUWATA, Y., TAKASHIMA, K. & CHIKASUE, R. 2015 A D3Q27 multiple-relaxation-time lattice Boltzmann method for turbulent flows. *Comput. Maths Applics.* **69**, 518–529.

SUGA, K., MATSUMURA, Y., ASHITAKA, Y., TOMINAGA, S. & KANEDA, M. 2010 Effects of wall permeability on turbulence. *Intl J. Heat Fluid Flow* **31**, 974–984.

SUGA, K., NAKAGAWA, Y. & KANEDA, M. 2017 Spanwise turbulence structure over permeable walls. *J. Fluid Mech.* **822**, 186–201.

SUGA, K., OKAZAKI, Y., HO, U. & KUWATA, Y. 2018 Anisotropic wall permeability effects on turbulent channel flows. *J. Fluid Mech.* **855**, 983–1016.

THOMSON, W. 1887 LXIII. On the division of space with minimum partitional area. *Lond. Edinb. Dublin Philos. Mag. J. Sci.* **24** (151), 503–514.

TOWNSEND, A.A. 1980 *The Structure of Turbulent Shear Flow*. Cambridge University Press.

VREMAN, A.W. & KUERTEN, J.G.M. 2014 Statistics of spatial derivatives of velocity and pressure in turbulent channel flow. *Phys. Fluids* **26** (8), 085103.

WHITAKER, S. 1986 Flow in porous media I: a theoretical derivation of Darcy's law. *Transp. Porous Med.* **1**, 3–25.

WHITAKER, S. 1996 The Forchheimer equation: a theoretical development. *Transp. Porous Med.* **25**, 27–61.

WHITE, B.L. & NEPF, H.M. 2007 Shear instability and coherent structures in shallow flow adjacent to a porous layer. *J. Fluid Mech.* **593**, 1–32.

ZIPPE, H.J. & GRAF, W.H. 1983 Turbulent boundary-layer flow over permeable and non-permeable rough surfaces. *J. Hydraul. Res.* **21** (1), 51–65.